



## **Sensitivity Study of the ITER Poloidal Polarimeter**

---

Taiki YAMAGUCHI, Yasunori KAWANO and Yoshinori KUSAMA

ITER Diagnostics Group  
Fusion Research and Development Directorate

**March 2008**

本レポートは日本原子力研究開発機構が不定期に発行する成果報告書です。  
本レポートの入手並びに著作権利用に関するお問い合わせは、下記あてにお問い合わせ下さい。  
なお、本レポートの全文は日本原子力研究開発機構ホームページ (<http://www.jaea.go.jp/index.shtml>)  
より発信されています。このほか財団法人原子力弘済会資料センター\*では実費による複写頒布を行っ  
ております。

〒319-1195 茨城県那珂郡東海村白方白根2番地4  
日本原子力研究開発機構 研究技術情報部 研究技術情報課  
電話 029-282-6387, Fax 029-282-5920

\*〒319-1195 茨城県那珂郡東海村白方白根2番地4 日本原子力研究開発機構内

This report is issued irregularly by Japan Atomic Energy Agency  
Inquiries about availability and/or copyright of this report should be addressed to  
Intellectual Resources Section, Intellectual Resources Department,  
Japan Atomic Energy Agency  
2-4 Shirakata Shirane, Tokai-mura, Naka-gun, Ibaraki-ken 319-1195 Japan  
Tel +81-29-282-6387, Fax +81-29-282-5920

© Japan Atomic Energy Agency, 2008

## Sensitivity Study of the ITER Poloidal Polarimeter

Taiki YAMAGUCHI<sup>※</sup>, Yasunori KAWANO and Yoshinori KUSAMA

Division of ITER Project  
Fusion Research and Development Directorate  
Japan Atomic Energy Agency  
Naka-shi, Ibaraki-ken

(Received October 11, 2007)

The poloidal polarimeter will be installed in the International Thermonuclear Experimental Reactor (ITER) to measure the profile of the toroidal current (safety factor) in the plasma core region. The number of viewing chords is restricted to about 15 channels because of the geometric capacity of diagnostic port plugs. In this work, we have studied the optimum viewing chord arrangement to achieve the high measurement accuracy for the first time. For the optimization of the viewing chord arrangement, as the first step, we have studied the sensitivity of the viewing chord arrangement on the current profile. We have proposed the new method for the sensitivity study, in which the Faraday rotation angle due to the toroidal current only is used as the sensitive index. As the result, the following sensitivities have been found. We have confirmed that the central viewing chords of the equatorial (EQ) port are sensitive to the central current density ( $j_0$ ). It has been also found that the central viewing chord in upper (UP) port is sensitive to the finite beta effect and not sensitive to  $j_0$ . We have shown that the combination of the central and the middle viewing chords of the EQ port is useful to distinguish the changes of  $j_0$  and the maximum toroidal current density in the case of the hollow current profile. Next, we have proposed the viewing chord arrangements which are sensitive to the current profiles of ITER operation scenarios. The method to make viewing chord arrangements which are sensitive to the change in the toroidal current profile around ITER operation scenarios has been also proposed.

Keywords: Poloidal Polarimeter, Current Profile, Sensitivity Study, Viewing Chord Arrangement, Magnetohydrodynamic Equilibrium Reconstruction, TOSCA, ITER

---

※ Post-Doctoral Fellow (Present Address: TECSYSTEM CO., LTD.,)

## ITER 用トロイダル偏光計測装置における感度解析

日本原子力研究開発機構 核融合研究開発部門

ITER プロジェクトユニット

山口 太樹※、河野 康則、草間 義紀

(2007 年 10 月 11 日 受理)

プラズマコア部の電流分布(安全係数分布)の計測を目的として、国際熱核融合実験炉(ITER)にトロイダル偏光計測装置が設置される予定である。ITER 用トロイダル偏光計測装置では、計測用ポートプラグの幾何学的制約のためレーザ視線数が制限される。本研究では、初めて、トロイダル電流分布同定の為に最適な視線配置を検討した。まず、視線最適化の第1段階として、視線位置のトロイダル電流分布に対する感度を明らかにした。従来の感度解析においては、トロイダル電流と外部コイルの両方に依存したファラデー回転角度を指標とした解析を行っていた。本研究では、トロイダル電流だけに依存したファラデー回転角度を新しい指標とした解析方法を提案した。この結果、中心電流密度に対してプラズマ中心付近を通る水平ポート視線の感度が高いことを、新しい指標を用いて確認することが出来た。また、プラズマ中心付近を通る上部ポート視線は中心電流密度に対して感度が低く、有限ベータ効果に対して感度が高いことを定量的に明らかにした。更に、凹状の電流分布を持つ負磁気シアプラズマにおいて、プラズマ中心付近とプラズマ中間領域付近のファラデー回転角度の組み合わせが、中心電流密度の変化と最大電流密度の変化を区別するために有効であることを示した。次に、ITER の運転シナリオに対して感度の高い視線配置案を提案した。この視線配置案では、トロイダル電流だけに依存したファラデー回転角度の分布形状を典型的に表す視線が選択された。また、トロイダル電流分布が運転シナリオから逸脱した場合、その変化に対して敏感な視線配置案の作成手法を提案した。ここでは、トロイダル電流だけに依存したファラデー回転角度が最も大きく変化する視線が選択された。



## Contents

1. Introduction -----	1
2. Calculation method of the Faraday rotation angle due to only the toroidal current -----	2
3. The mechanisms of the sensitivities -----	3
3.1 Candidate viewing chords -----	3
3.2 Sensitivity to the central toroidal current density -----	3
3.3 Sensitivity to the finite beta effect -----	4
3.4 Sensitivity to the negative magnetic shear -----	5
3.5 Consideration of insensitivities at each viewing chord region -----	5
4. Proposal of the viewing chord arrangement for the ITER operation scenario -----	6
4.1 The method to make the viewing chord arrangement -----	6
4.2 Initial viewing chord arrangement for the ITER operation scenario -----	7
4.2.1 Inductive operation scenario II -----	7
4.2.2 Non-inductive operation scenario -----	8
5. The viewing chord arrangement to measure the change in the current profile around the ITER operation scenario -----	8
5.1 Inductive operation scenario II -----	8
5.2 Non-inductive operation scenario -----	9
6. Discussion -----	9
7. Future works -----	10
8. Summary -----	10
Acknowledgements -----	11
References -----	11

目 次

1. はじめに .....	1
2. トロイダル電流分布のみに依存したファラデー回転角度の計算手法 .....	2
3. 感度の機構 .....	3
3.1 視線の候補 .....	3
3.2 中心トロイダル電流密度に対する感度解析 .....	3
3.3 有限ベータ効果に対する感度解析 .....	4
3.4 負磁気シアにおける感度解析 .....	5
3.5 各視線領域の鈍感さに関する検討 .....	5
4. ITER 運転シナリオにおける視線配置の提案 .....	6
4.1 視線配置案の作成手法 .....	6
4.2 ITER 運転シナリオにおける視線配置の初期案 .....	7
4.2.1 誘導運転シナリオⅡ .....	7
4.2.2 非誘導運転シナリオ .....	8
5. ITER 運転シナリオから電流分布が変化した場合の計測に適した視線配置 .....	8
5.1 誘導運転シナリオⅡ .....	8
5.2 非誘導運転シナリオ .....	9
6. 議論 .....	9
7. 今後の予定 .....	10
8. まとめ .....	10
謝辞 .....	11
参考文献 .....	11

## 1. Introduction

Identification of the toroidal current profile,  $j(r)$ , or the safety factor,  $q(r)$ , is necessary for the plasma stability analyses, transport analyses and the control of  $j(r)$  or  $q(r)$ . Three types of diagnostic device will be installed in the International Thermonuclear Experimental Reactor (ITER) to measure  $j(r)$  or  $q(r)$ , which are the poloidal polarimeter (core region), the Motional Stark Effect (MSE) polarimeter (peripheral region) and magnetic probes and coils.

For the poloidal polarimeter, proposed wavelength of the laser beam is 118.8  $\mu\text{m}$  ( $\text{CH}_3\text{OH}$  laser) [1]. The laser beams passing through the plasma are reflected back along the same path by retroreflectors. The Faraday rotation angle of the polarization plane of each beam is induced by the poloidal field inside the plasma. The principal items to be studied for developing the poloidal polarimeter are followings:

- laser transmission systems for the equatorial port and the upper port
- plasma facing mirrors (first mirrors and retroreflectors)
- upper port plug (Japan will procure the upper port plug for the poloidal polarimeter)
- laser systems
- detection systems

The viewing chord arrangement affects all items listed above. The arrangements should be optimized to achieve the accurate identification of  $j(r)$  because the number of viewing chords is limited. Therefore the determination of viewing chord arrangement is a high priority issue at the beginning of the design of the poloidal polarimeter.

The following results related to the viewing chords had been obtained in previous reports for the ITER poloidal polarimeter.

- The number of viewing chords is restricted to about 9 channels in the equatorial (EQ) port and about 6 channels in the upper (UP) port because of the geometric capacity of port plugs [1].
- The central viewing chords of EQ port are sensitive to the central safety factor,  $q_0$  [2, 3]. The sensitivity is analyzed based on the Faraday rotation angle which includes the effects of the magnetic field due to  $j(r)$  and the magnetic field due to external coils.
- The viewing chords of UP port are sensitive to the Shafranov shift (qualitative understanding).

In the above previous reports, the optimum viewing chord arrangement had not been studied. In this work, we have studied the optimum viewing chord arrangement for the first time since it is a starting condition of the over all system design as mentioned before.

There are two points of view for the optimization of the viewing chord arrangement. One is the identification of  $j(r)$  or  $q(r)$  of plasmas with the required resolution and accuracy. Those requirements are shown in Table 1. For example, the spatial resolution of  $a/20$ , where  $a$  is the minor radius, and the accuracy of 10 % are required for the identification of  $q(r)$  in the coverage region  $0.5 < q < 5$  [4]. Another point of view is to meet the engineering requirements. The detailed considerations of the optical system and components inside port plugs and inside the vacuum vessel are necessary to satisfy the engineering requirements. However the second point is out of scope of this paper.

The quantitative accuracy of the identified  $j(r)$  can be evaluated by the Magnetohydrodynamic (MHD) equilibrium reconstruction method. One idea to know the optimum viewing chord arrangement is the evaluations of  $j(r)$  by the MHD equilibrium reconstruction method for all combinations of viewing chords. But it is actually impossible because the number of the arrangement patterns is very large ( $\sim 10^{10}$  patterns). Therefore we have divided the optimization study in two steps. First step is the making the candidate viewing chord arrangements based on the result of the sensitivity study [5]. The mechanisms of the sensitivities should be also understood in this step. The second step is the evaluation of the quantitative accuracy of  $j(r)$  using the MHD equilibrium reconstruction method. The viewing chords arrangement given by the first step will be used in this step. We focus on the first step in this paper.

## 2. Calculation method of the Faraday rotation angle due to only the toroidal current

The Faraday rotation angle along a viewing chord,  $F$ , is approximately shown as the following equation [6]:

$$F = \frac{e^3 \lambda^2}{8\pi^2 \epsilon_0 m_e^2 c^3} \int n_e B_{\parallel} dl \quad (2.1.1)$$

where  $\lambda$  is the wavelength of the laser,  $m_e$  is the mass of electron,  $n_e$  is the electron density,  $\epsilon_0$  is the dielectric constant of vacuum,  $B_{\parallel}$  is the magnetic field parallel to the direction of the viewing chord.  $B_{\parallel}$  includes the magnetic fields due to the plasma current  $B_{\parallel}^{pl}$  and due to the external coils  $B_{\parallel}^{vac}$ . Therefore eq. (1) can be written as:

$$F = \frac{e^3 \lambda^2}{8\pi^2 \epsilon_0 m_e^2 c^3} \int n_e B_{\parallel}^{pl} dl + \frac{e^3 \lambda^2}{8\pi^2 \epsilon_0 m_e^2 c^3} \int n_e B_{\parallel}^{vac} dl \quad (2.1.2).$$

The first term and the second term correspond to the Faraday rotation angles due to the plasma current and the external coils, respectively. By denoting the former as  $F^{PL}$  and denoting the latter as  $F^{EXT}$ , the (2.1.2) can be written as:

$$F = F^{PL} + F^{EXT} \quad (2.1.3).$$

$F$  had been used as the index of the sensitivities in the previous reports [2, 3]. But  $F^{PL}$  should be used when the objective is to understand the sensitivity between the viewing chord positions and  $j(r)$ . Therefore, in this study,  $F^{PL}$  has been used as the index of the sensitivities.

$B_{\parallel}^{pl}$  and  $B_{\parallel}^{vac}$  are given by the result of the MHD equilibrium calculation. As the MHD equilibrium calculation code, we have used ‘‘Tokamak Operation Scenario and Circuit Analysis code (TOSCA)’’, which had been used for the considerations of the operation scenarios of ITER. Although the Faraday rotation

angle is a function of the electron density also, we assumed the fixed electron density profile as  $n_e(\rho) = 10^{19} + 10^{20} (1 - \rho^{10}) \text{ m}^{-3}$  (see Fig. 1), with  $\rho$  the normalized minor radius, so that the sensitivity only of the toroidal current profile can be known. In ITER,  $n_e(\rho)$  can be measured by the toroidal interferometer/polarimeter system, the Thomson scattering systems, and the measurement of the ellipticity due to the Cotton-Mouton effect using the poloidal polarimeter.

### 3. The mechanisms of the sensitivities

#### 3.1 Candidate viewing chords

The EQ port and the UP port are used for launching the laser beams into the vacuum vessel of ITER and receiving the returning laser beams [1]. Figure 2 shows the poloidal cross section of the ITER vacuum vessel with all candidate viewing chords. The arrangement of each viewing chord has been determined by the positions of retroreflectors, which are assumed to be installed inside the remote handling slots of the blanket modules in this study, and possible first mirror positions. The viewing chords of 24 channels for the EQ port and of 21 channels for the UP port have been picked up. At the existing design, the possible numbers of viewing chords will be restricted to about 9 channels for the EQ port and about 6 channels for the UP port because of the geometric capacity of port plugs [1]. The positions of viewing chords in the EQ port and in the UP port are identified with the angles of  $\theta$  and  $\xi$ , respectively (Fig. 2).

#### 3.2 Sensitivity to the central toroidal current density

Figure 3 shows the inputs and results of calculation using TOSCA. The central toroidal current density,  $j_0$ , is scanned. The net toroidal current  $I_p = 15 \text{ MA}$ , the position and the shape of last closed flux surface (LCFS), the poloidal beta value  $\beta_p$  are fixed. The fixed parameters and one of the toroidal current profiles (bold line in Fig. 3) are same as those of the ITER design scenario II (inductive operation) at the start of the burn phase (S2-SOB). Figure 4 shows  $F$  and  $F^{\text{pl}}$ . The definition of the viewing chord angles  $\theta$  and  $\xi$  are shown in Fig. 2. We can see that the differences between  $F$  and  $F^{\text{pl}}$  are about 1.7 times for the EQ chords and 1.5 times for the UP chords.

In the Fig. 5, the definition of the central slope is shown. The central slope of  $F^{\text{pl}}$  is defined by  $dF^{\text{pl}}/d\theta$ , where  $dF^{\text{pl}}$  is a difference between  $F^{\text{pl}}$  of viewing chords of the EQ port at  $\theta = -15 \text{ deg.}$  and that at  $11 \text{ deg.}$ . In the previous works[2, 3], it had been reported that (i) the relationship between the reciprocal of the central safety factor  $q_0^{-1}$  and the central slope of the  $F$  is linear and (ii) the dependence of the toroidal current profile on the proportional coefficient is weak. At first, those sensitivities have been confirmed by our analyses as shown in Fig. 6. In Fig. 6, three different  $I_p$  (11, 13 and 15 MA) are examined and other conditions are same as those for Fig. 3. We can confirm that the relationship between  $q_0^{-1}$  and the slope of the  $F$  is linear. Next, we have studied the dependence of  $q_0$  on the slope of  $F^{\text{pl}}$  (Fig. 7). From this analysis, it is shown that (i) the relationship between  $q_0^{-1}$  and the slope of the  $F^{\text{pl}}$  is also linear and (ii) the dependence

of the toroidal current profile on the proportional coefficient is not weak. The effect of the external field is also included in  $q_0$ . The dependence of  $j_0$  on the central slope of  $F^{\text{pl}}$  in the EQ port is shown in Fig. 8. From above analyses, it can be said with good reliability that the central viewing chords of the EQ port are sensitive to  $j_0$ .

### 3.3 Sensitivity to the finite beta effect

The sensitivity of the finite beta effect is studied in this section. The Pfirsch-Schlüter (P.S.) current,  $j_{\text{ps}}$ , is induced by the finite beta effect (see Fig. 9). The P.S. current is described as the following:

$$j_{\text{ps}} \propto \frac{q}{B} \frac{\partial(p_{\perp} + p_{\parallel})}{\partial r} \cos \eta \quad (3.3.1)$$

where  $p_{\perp}$  is the plasma pressure perpendicular to the magnetic field,  $p_{\parallel}$  is that parallel to the magnetic field and  $\eta$  is the poloidal angle. In the case of the isotropic pressure, it is shown as the following:

$$j_{\text{ps}} \propto \frac{q}{B} \frac{\partial p}{\partial r} \cos \eta \quad (3.3.2).$$

The sensitivity of the finite beta effect means the sensitivity of the magnetic field due to the P.S. current.

Figures 10 and 11 show the calculated results of TOSCA, for which the  $j(r)$  without the P.S. current is fixed to investigate the effect of the P.S. current. The net plasma current,  $I_p$ , and the position and the shape of LCFS are also fixed. The poloidal beta value  $\beta_p$  is scanned, i.e. 0.05, 0.3, 0.65 and 0.8. Figure 12 shows the calculated  $F^{\text{pl}}$  in the EQ port and the UP port. The dependence of  $\beta_p$  on the central slope of  $F^{\text{pl}}$  in the EQ port is shown in Fig. 13. The linear relationship between the  $j_0$  and the slope is broken when  $\beta_p$  changes. The additional information relating to  $\beta_p$  is necessary because it is difficult to distinguish the effect due to the change in  $j_0$  and due to change in  $\beta_p$  only by central viewing chords of the EQ port. Moreover the P.S. current depends not only on the average beta value but also on the pressure profile. The diagnostics relating to the pressure profile, which measure the profiles of the electron density, the electron temperature, the ion temperature and the mean effective ion charge ( $Z_{\text{eff}}$ ), can take the information of P.S. current. But the fewer diagnostics for the MHD reconstruction is attractive. Furthermore the P.S. current depends on the neutral beam pressure and the pressure anisotropy [7]. However the measurement of the anisotropic pressure profile is difficult. In order to distinguish the effect due to the change in  $j_0$  and due to change in  $\beta_p$ , the viewing chords of the UP port will be useful because the viewing chords of the UP port are sensitive to the P.S. current and not sensitive to the toroidal current profile. But it had been only a qualitative estimation. The sensitivities of  $j_0$  and of  $\beta_p$  on the viewing chords of the UP port have been quantitatively evaluated in this study. Figure 14 shows the dependence of  $F^{\text{pl}}$  of the central chord in the UP port ( $\xi \approx 0$ ) on the changes of  $\beta_p$  and  $j_0$ . The  $\beta_p, j_0$  and  $F^{\text{pl}}$  at ITER design scenario S2-SOB are used as the reference ( $\Delta F^{\text{pl}} = 0$ ) and the

differences from that are shown.  $\Delta\beta_p$  and  $\Delta j_0$  are defined as the relative difference from those of S2-SOB. The change in  $\Delta\beta_p = 10\%$  induces 2.7 deg. of  $\Delta F^{pl}$  although the change in  $\Delta j_0 = 10\%$  induces only 0.7 deg. of  $\Delta F^{pl}$ . Therefore it was found that the central chord of the UP port is sensitive to  $\beta_p$  and less sensitive to  $j_0$ .

The P.S. current induces the vertical magnetic field. Then the vertical magnetic field induces the Shafranov shift. The Faraday rotation angle of each viewing chord is affected by the vertical magnetic field and the Shafranov shift. The comparison of those effects is discussed in Sec. 6.2.

### 3.4 Sensitivity to the negative magnetic shear

The plasmas in above analyses have the normal magnetic shear. The sensitivity to the hollow type toroidal current profiles, which construct the negative magnetic shear, has been also studied. The example of that is shown in Fig. 15 (a) in which  $I_p$ ,  $\beta_p$ , the position and the shape of LCFS and the pressure profile are same. Figure 15 (b) shows the difference of magnetic field distributions due to current profiles shown in Fig. 15 (a). Figure 15 (c) shows the Faraday rotation angle of EQ chords, which is calculated by the difference of the magnetic field shown in Fig. 15 (b). The slope of middle viewing chords is larger than the slope of central viewing chords. The reason is that the magnetic field difference near the central region is small and the difference near the middle region is large (see Fig. 15 (b)). Figure 16 shows an example in the case of the normal shear. The slope of middle viewing chords is smaller than the slope of central viewing chords. Figures 17 and 18 show the results of current profile scans which are  $j_0 / j_{\max}$  scan (from broad to hollow shape) and  $j_0$  scan (from broad to peak shape), where  $j_{\max}$  is the maximum toroidal current density, the central slope is defined as same as that shown in Fig. 5 and the middle slope is defined as the slope between  $\theta = -35$  deg. and  $-26$  deg. as shown in Fig. 5. The both slopes of  $\Delta F^{pl}$  at the central region and at the middle region increase in both cases of  $j_0$  increase and  $j_0 / j_{\max}$  decrease. But the relative relations between the central slope and the middle slope are different, namely, the slope of  $\Delta F^{pl}$  at the central region is larger than the slope of the middle region in the case of  $j_0$  increase, whereas it is an opposite relationship in the case of  $j_0 / j_{\max}$  scan. Therefore the combination of the central and the middle chords is useful to distinguish the change in  $j_0$  and  $j_0 / j_{\max}$ .

### 3.5 Consideration of insensitivities at each viewing chord region

The sensitivities between the current profiles and the viewing chords regions are summarized in Fig. 19. The current profiles are scanned by changing the parameters  $j_0$ ,  $\beta_p$  and  $j_0 / j_{\max}$ . Note that other conditions are fixed when one parameter is scanned. The viewing chord region is divided into the center region of the EQ port viewing chords, the central region of the UP port viewing chords and the middle region of the EQ port viewing chords. The central slope and middle slope of viewing chords in the EQ port have same definitions with those shown in Fig. 5. Those slopes are used as the sensitive index for the central and the middle region of EQ port viewing chords. The central viewing chord of the UP port defined in Sec. 3.3 is

used as the sensitive index for the central region of the UP port viewing chords. The strength of the gradient of each graph means the strength of the sensitivity. The detailed explanations of sensitivities were described in Sec. 3.2, 3.3 and 3.4. Not only the sensitivities but also the insensitivities are important for the MHD equilibrium reconstruction to escape from the ill-posed problem. The following insensitivities can be seen from Fig. 19 :

- The sensitivities of the central UP port viewing chord other than the sensitivity on  $\beta_p$  are weak.
- The sensitivity of the central EQ port viewing chord on  $\beta_p$  is weak.
- The sensitivity of the middle EQ port viewing chord on  $\beta_p$  is weak.

#### 4. Proposal of the viewing chord arrangement for the ITER operation scenario

##### 4.1 The method to make the viewing chord arrangement

There are 4 typical scenarios for ITER operations as the followings:

1. Inductive operation I : operation with heating during current ramp-up
2. Inductive operation II : operation without heating during current ramp-up
3. Hybrid operation
4. Non-inductive operation : weak negative magnetic shear operation.

Here we propose the viewing chord arrangements for inductive operation II and non-inductive operation. The method to make the viewing chord arrangements is shown in this section.

The comparison among  $F$ ,  $F^{\text{EXT}}$  and  $F^{\text{PL}}$ , which are calculated from the equilibrium of non-inductive operation scenario at the start of the burn phase as the example, are shown in Fig. 20. The ratio of  $F^{\text{EXT}}$  to  $F$  is about 50%. The profile shapes of  $F$  and  $F^{\text{PL}}$  are different, for example, the central slopes of  $F$  and  $F^{\text{PL}}$  are much different. The peak positions of  $F$  and  $F^{\text{PL}}$  are also different. There is a possibility to select the unsuitable viewing chords if  $F$  is used as the sensitive index. Therefore we propose the method to make the viewing chord arrangements using  $F^{\text{PL}}$ .

The  $F^{\text{pl}}$  profile for the inductive operation scenario at  $I_p=11.5\text{MA}$  is shown in Fig. 21. The method to make the viewing chord arrangements of the EQ port is explained based on Fig. 21.

Step A : The two viewing chords which sandwich  $R_{ax}$  are selected to put an importance to detect  $j(r)$  near the plasma center.

Step B : The viewing chord which has the maximum  $F^{\text{pl}}$  is selected because it is a typical point to show the  $F^{\text{pl}}$  profile.

Step C : If there is a single inflection point between the viewing chords selected by Step A and by Step B, see Example 1 and Fig. 21. If there are plural inflection points, see Example 2 and Fig. 22.

Example 1 : A straight line is drawn to link two points which are selected by Step A and B. The viewing chord, whose  $F^{\text{pl}}$  shows the largest difference from the straight line, is selected.



Example 2 : A straight line is drawn to link two points. One point is selected by Step A. Another point is next inside point to the point selected by Step B. The viewing chord, in which  $F^{\text{pl}}$  shows the largest difference from the straight line, is selected.

Step D : Step B and C are done for the lower side from a equator.

The 6 viewing chords of the EQ port have been selected by this method.

The method to make the viewing chord arrangements of the UP port is a future work. One objective of the viewing chords of the UP port is the detection of the Shafranov shift. The chords should be arranged near  $R_{\text{ax}}$  in order to detect the Shafranov shift. As another objective for the viewing chords of the UP port, there is a possibility to detect the current density in the peripheral region. The possibility is discussed in Sec. 6.

## 4.2 Initial viewing chord arrangement for the ITER operation scenario

### 4.2.1 Inductive operation scenario II

Figure 23 shows the time evolution of  $I_p$  in the case of the inductive scenario II. Figure 24 shows the LCFS and the current profiles at eight time points which are shown by the circles in Fig. 23. Figure 25 shows  $F^{\text{PL}}$  profiles at three time points numbered in Fig. 23. The vertical lines mean the selected viewing chord positions by the method described in Sec. 4.1. The time shown as No. 3 is a start of the burning phase. From the time No. 1 to No. 2, the viewing chord positions selected by Step B and C, are shifted to the outboard side because the plasma boundary is expanded. From the time No. 2 to No. 3,  $j(r)$  becomes broader although the plasma boundary is almost same. Therefore the viewing chord position of Step B is shifted to the outboard side. On the other hand, the viewing chord position of Step C is shifted to the inboard side because  $F^{\text{PL}}$  profiles changes to a little concave profile in the region of  $-50 \text{ deg.} < \theta < 0 \text{ deg.}$ . The vertical lines in Fig. 26 shows  $F^{\text{PL}}/I_p$  profiles at all time points with selected viewing chord positions. The bold vertical lines show the selected viewing chord positions at the burning phase. The candidate viewing chords of the EQ port could be restricted to 12 channels from all candidates (24 channels). The high priority may be given to the candidate viewing chords at the burning phase (6 channels). The actually possible number of channels in the EQ port had been estimated to be  $\sim 9$  channels in the previous report [1]. If the candidate viewing chords at the burning phase were selected, the accuracy during the other phases would be decreased. In order to prevent the decrease of the accuracy, the remaining 3 channels should be arranged effectively. The region, where the remaining channels should be arranged, is shown with a symbol ‘ \* ’ in Fig. 26. In the future work, the detailed viewing chord positions in the region will be determined by the quantitative accuracy evaluation based on the MHD equilibrium reconstruction method.

#### 4.2.2 Non-inductive operation scenario

The same analyses as those in Sec. 4.2.1 were carried out in the case of the non-inductive scenario. The results are shown from Figure 27 to Fig. 30. The plasma boundary is expanded from the time No. 1 to No. 2. The time shown as No. 3 means a start of the burning phase. The viewing chord positions selected by Step B and C, are shifted to the outboard side by the change in the plasma boundary. The toroidal current profile becomes a hollow shape from the time No. 2 to No. 3 although the plasma boundary is almost same. The viewing chord position of Step B is shifted to the outboard side. The viewing chord position of Step C is shifted to the inboard side because  $F^{\text{PL}}$  near the  $\theta \sim 20$  deg. decreases. From Fig. 30, it is found that the number of candidate viewing chord arrangement is more than that for the inductive operation scenario. The reason is a significant change in the current profile. In order to prevent the decrease of the accuracy at phases before the burning phase, the additional viewing chords are effective in the region shown as ‘ \* ’ in Fig. 30.

### 5. The viewing chord arrangement to measure the change in the current profile around the ITER operation scenario

Until the previous chapters, we have mainly focused on  $j(r)$  of the ITER operation scenarios. Since there is a possibility of the change in  $j(r)$  around the operation scenario, it is important to measure the difference of  $j(r)$  from the operation scenario. The method to arrange the viewing chords, which is sensitive to the difference of  $j(r)$  from the operation scenario, is described in this chapter.

#### 5.1 Inductive operation scenario II

The change in the current profile around the inductive scenario II at the start of the burn phase was considered on the condition of fixed  $I_p$ . The profiles of  $j(r)$  and  $q(r)$  are shown in Fig. 31 (a) and (b), respectively. The bold lines mean  $j(r)$  and  $q(r)$  in the inductive scenario II at the start of the burn phase. In this scan, the  $q(r)$  is increased in most region. The  $F^{\text{PL}}$  profile is shown in Fig. 31 (c). The  $\Delta F^{\text{PL}}$  is defined as the difference between  $F^{\text{PL}}$  for the current profile of the inductive scenario II at start of the burn phase and  $F^{\text{PL}}$  for the changed current profile. The  $\Delta F^{\text{PL}}$  profile is shown in Fig. 31 (d). In Fig. 31 (d), adequate channels to measure the current profile of the operation scenario, which are selected in Sec. 5.1, are also shown (vertical bold broken lines). The vertical bold line in Fig. 31 (d) shows the maximum point of the  $\Delta F^{\text{PL}}$  profile. The viewing chord, which has the maximum point of the  $\Delta F^{\text{PL}}$  profile, is adequate to detect the change in the current profile because the viewing chord at the maximum point of the  $\Delta F^{\text{PL}}$  profile is the most sensitive to the change in  $j(r)$ .

In the next analysis, the magnetic shear is scanned on the condition of fixed  $q_0$  and  $I_p$ . The profiles of  $j(r)$  and  $q(r)$  are shown in Fig. 32 (a) and (b). The bold lines mean them in the inductive scenario II at the start of the burn phase. In this scan, a weak magnetic shear region is expanded. The  $F^{\text{PL}}$  profile and the

$\Delta F^{\text{PL}}$  profile are shown in Fig. 32 (c) and (d). The vertical bold line in Fig. 32 (d) shows the maximum point of the  $\Delta F^{\text{PL}}$  profile.

## 5.2 Non-inductive operation scenario

In this section, the change around the current profile of the non-inductive scenario is considered on the condition of fixed  $I_p$ . The profiles of  $j(r)$  and  $q(r)$  are shown in Fig. 33 (a) and (b). The bold lines mean them in the non-inductive scenario at the start of the burn phase. In this scan, the  $q(r)$  is increased in most region. The  $F^{\text{PL}}$  profile and the  $\Delta F^{\text{PL}}$  profile are shown in Fig. 33 (c) and (d), respectively. The vertical bold line in Fig. 33 (d) shows the maximum point of the  $\Delta F^{\text{PL}}$  profile.

In the next analysis, the magnetic shear is scanned on the condition of fixed  $q_{\text{min}}$  and  $I_p$ . The profiles of  $j(r)$  and  $q(r)$  are shown in Fig. 34 (a) and (b). The bold lines mean them in the non-inductive scenario at the start of the burn phase. The  $F^{\text{PL}}$  profile and the  $\Delta F^{\text{PL}}$  profile are shown in Fig. 34 (c) and (d), respectively. The vertical bold line in Fig. 34 (d) shows the maximum point of the  $\Delta F^{\text{PL}}$  profile.

The method, which selects the viewing chord at the maximum point of the  $\Delta F^{\text{PL}}$  profile, is useful to pick up the candidate viewing chords to detect the change in  $j(r)$ . In the future work, these viewing chords will be considered based on the MHD equilibrium reconstruction method.

## 6. Discussion

We discuss about the mechanism of the strong sensitivity to the finite beta effect on the viewing chords in the UP port (see Fig. 14 (a)). The mechanism of the finite beta effect on the  $F^{\text{PL}}$  of the viewing chords in the UP port is shown in Fig. 35. The P.S. current depends on the average beta, the pressure profile and the pressure anisotropy. The P.S. current induces the vertical magnetic field,  $B_z$ . The position of the magnetic axis,  $R_{\text{ax}}$ , is shifted by the  $B_z$ . There are two possibilities as the reason of the strong sensitivity to the finite beta effect on the viewing chords in the UP port; (i) The vertical magnetic field due to the P.S. current affects directly the central viewing chord in the UP port (see Fig. 36 (i)), and (ii) the relative position between the viewing chord and the magnetic axis are changed by the Shafranov shift (see Fig. 36 (ii)). It is interesting to compare the magnitude of those effects. For the strict comparison, two MHD equilibria, where the magnetic surface configurations including  $R_{\text{ax}}$  positions are same (the effects of (ii) are same) but the beta values are different (the effects of (i) are different), are necessary. But those equilibria are difficult to make. The shift of magnetic axis,  $\Delta R_{\text{ax}}$ , is different with the shift of the geometric center of LCFS,  $\Delta R_0$ , in the case the beta value increases (see Fig. 37 (a)), whereas  $\Delta R_{\text{ax}}$  and  $\Delta R_0$  are almost same in the case external coil currents change (see Fig. 37 (b)). Therefore the LCFS positions are different when the magnetic axis positions are same and the beta values are different. Here we assume that the effect of  $R_{\text{ax}}$  shift by external coil currents is due to the effect of (ii) although this is a rough estimation. Figure 38 shows the relationship between  $R_{\text{ax}}$  and  $F^{\text{pl}}$ , in which the  $R_{\text{ax}}$  shift is induced by the finite beta effect and the

external coils. The painted patterns mean the difference of  $\beta_p$  and the shapes of symbols show the difference of  $R_{ax}$  by external coils. The change in  $\Delta\beta_p = 0.1$  induces  $\Delta F^{pl} \approx 4$  deg., i.e. it is a sum of effects of (i) and (ii), and  $\Delta R_{ax} \approx 0.02$  m (see Fig. 38 “A”). The change in  $F^{pl}$  is about 3 deg. if  $\Delta R_{ax} \approx 0.02$  m is induced by external coil’s current, i.e. it is assumed as the effect of (ii) (see Fig. 38 “B”). Therefore, from this analysis, it is thought that the effect of (ii) is much larger than that of (i).

## 7. Future works

The future works to be done are shown as the followings.

- The development of the MHD equilibrium reconstruction code
- The quantitative evaluation of the accuracy of the identified  $j(r)$  for the ITER operation scenarios at the burning phase

The viewing chords, which are sensitive to the operation scenarios at the burning phase, have been selected in this study. The MHD equilibrium reconstruction of  $j(r)$  at the burning phase will be carried out and the quantitative accuracy of the identified  $j(r)$  will be evaluated.

- The proposal of the viewing chord arrangements which are optimized for each operation scenario

The viewing chord arrangement, which is sensitive to  $j(r)$  at the burning phase, will be used in the above future work. The accuracy at the other phases will be decreased because the sensitivities on  $j(r)$  at the other phases are small. The quantitative accuracy of the reconstructed  $j(r)$  must be evaluated at the other phases. The viewing chords of 6 channels were selected for the candidate EQ port chords in this study. The remaining channels should be arranged effectively in order to prevent the decrease of the accuracy if the accuracy decreases drastically at the other phases. The candidate viewing chords to be arranged effectively have been known in this study. The detailed arrangement will be determined by the quantitative evaluation based on the MHD equilibrium reconstruction.

- The proposal of the viewing chord arrangements which are optimized for each operation scenario
- The proposal of single arrangement of viewing chord, which is optimized as the poloidal polarimeter

Some of items listed above were investigated. The results were reported in Ref. [8].

## 8. Summary

For the optimization of the viewing chord arrangement, as the first step, we have studied the sensitivity of the viewing chord arrangement on the toroidal current profile. The Faraday rotation angle,  $F$ , which depends on the toroidal current and the external coils’ current, had been used as the sensitive index in the previous studies by other groups. We have proposed the new method for the sensitivity study, in which the Faraday rotation angle due to the toroidal current only,  $F^{pl}$ , is used as the sensitive index. As the result, the following sensitivities are found.

- We have confirmed the sensitivity with a better reliability by showing the linear dependence of  $j_0$  on the central slope of  $F^{\text{pl}}$ .
- We have studied the sensitivity of the finite beta effect. The linear dependence of  $j_0$  on the central slope of  $F^{\text{pl}}$  is broken when  $\beta_p$  changes. We have shown that the central chord of the UP port is useful to distinguish the effect due to the change in  $j_0$  and due to change in  $\beta_p$ . The change in  $\Delta\beta_p = 10\%$  induces 2.7 deg. of  $\Delta F^{\text{pl}}$ , whereas the change in  $\Delta j_0 = 10\%$  induces only 0.7 deg. of  $\Delta F^{\text{pl}}$ .
- We have shown that the combination of the central and the middle viewing chords of the EQ port is useful to distinguish the changes of  $j_0$  and the maximum toroidal current density,  $j_{\text{max}}$ , in the case of the hollow current profile. The slope of  $\Delta F^{\text{pl}}$  at central region is larger than the slope of middle region in the case of  $j_0$  increase, whereas it has a opposite dependence in the case of  $j_0 / j_{\text{max}}$  scan.

Next, we have proposed the viewing chord arrangements which are sensitive to the toroidal current profiles of ITER operation scenarios. The viewing chords are selected for the inductive operation II and the non-inductive operation. The method to select the viewing chords, which is based on  $F^{\text{pl}}$ , has been proposed. The candidate viewing chords of the EQ port have been restricted to 12 channels from all candidates (24 channels) for the inductive operation II and have been restricted to 17 channels for non-inductive operation. The high priority may be given to the candidate viewing chords at the burning phase (6 channels). If the candidate viewing chords at the burning phase were selected, the accuracy during the other phases would be decreased. In order to prevent the decrease of the accuracy, the remaining 3 channels should be arranged effectively. The region, where the remaining channels should be arranged, has been found in this study.

The method to arrange the viewing chords, which is sensitive to the change in  $j(r)$  around the ITER operation scenarios, has been proposed. The viewing chord, which has the maximum point of the  $\Delta F^{\text{pl}}$  profile, is adequate to detect the change in the current profile. The maximum points of the  $\Delta F^{\text{pl}}$  profile have been picked up in the case of the change in  $q(r)$  in a large region and in the case of the change in the magnetic shear.

## Acknowledgements

The authors would like to express their thanks to Drs M. Sugihara and H. Fujieda for useful discussion about the MHD equilibrium calculations.

## References

- [1] A.J.H. Donné et al. : "Poloidal polarimeter for current density measurements in ITER", Rev. Sci. Instrum, 75, 4694 (2004).
- [2] A.J.H. Donné et al. : "Polarimetry for poloidal field measurements", in Diagnostics for Experimental Thermonuclear Fusion Reactors 2, edited by P. E. Stott et al. (Plenum, New York, 1998) p.203.
- [3] C. Nieswand : "Faraday rotation calculations for a FIR polarimeter on ITER", in Diagnostics for Experimental Thermonuclear Fusion Reactors 2, edited by P. E. Stott et al. (Plenum, New York, 1998)

p.213.

- [4] A.J.H. Donné et al. : “Progress in the ITER Physics Basis, Chapter 7: Diagnostics”, Nucl. Fusion, 47, S337 (2007)
- [5] T. Yamaguchi et al. : “Sensitivity study for the optimization of the viewing chord arrangement of the ITER poloidal polarimeter”, Plasma and Fusion Research (in press)
- [6] D. Veron, in *Infrared and Millimeter Waves* (Academic, New York, 1979), 2, p. 67
- [7] T. Yamaguchi et al. : “Measurement of anisotropic pressure using magnetic measurements in LHD”, Nucl. Fusion, 45, L33 (2005).
- [8] T. Yamaguchi et al. : “Optimization of the viewing chord arrangement of the ITER poloidal polarimeter”, Proc. 34th Eur. Conf. on Plasma Physics (Warsaw, 2007), P5.078, (in press)

Table 1 Specification for the safety factor measurements on ITER [2].  $a$  is the minor radius of the plasma boundary and  $q_{\min}$  is the minimum value of the safety factor.

Parameter	Range	Time Resolution	Spatial Resolution	Accuracy
$q(r)$	0.5-5	10 ms	$a/20$	10%
$r(q = 1.5, 2)/a$	5-TBD	10 ms	$a/20$	0.5
	0.3-0.9	10 ms	-	50mm/a
$r(q_{\min})/a$	0.3-0.7	1 s	-	50mm/a

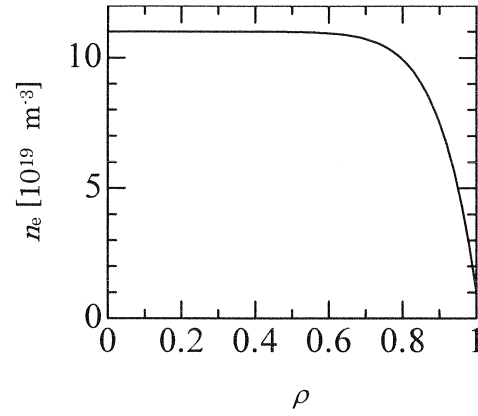


Fig. 1 The electron density profile used for the calculation of the Faraday rotation angle in this study.

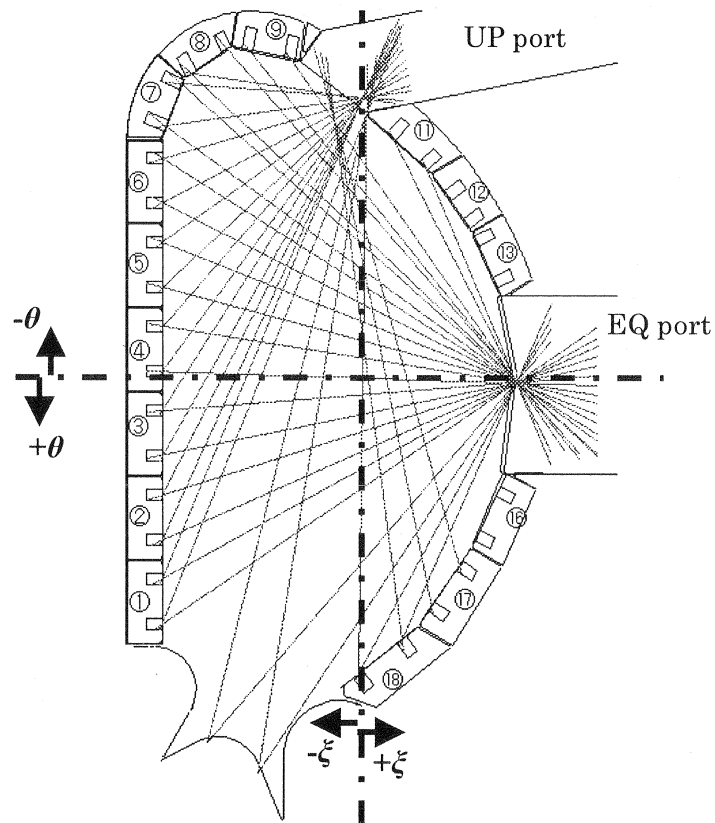


Fig. 2 All candidate viewing chords of the ITER poloidal polarimeter. The viewing chord positions in the EQ port is shown as the angle  $\theta$  and the viewing chord positions in the UP port is identified with the angle  $\xi$ .



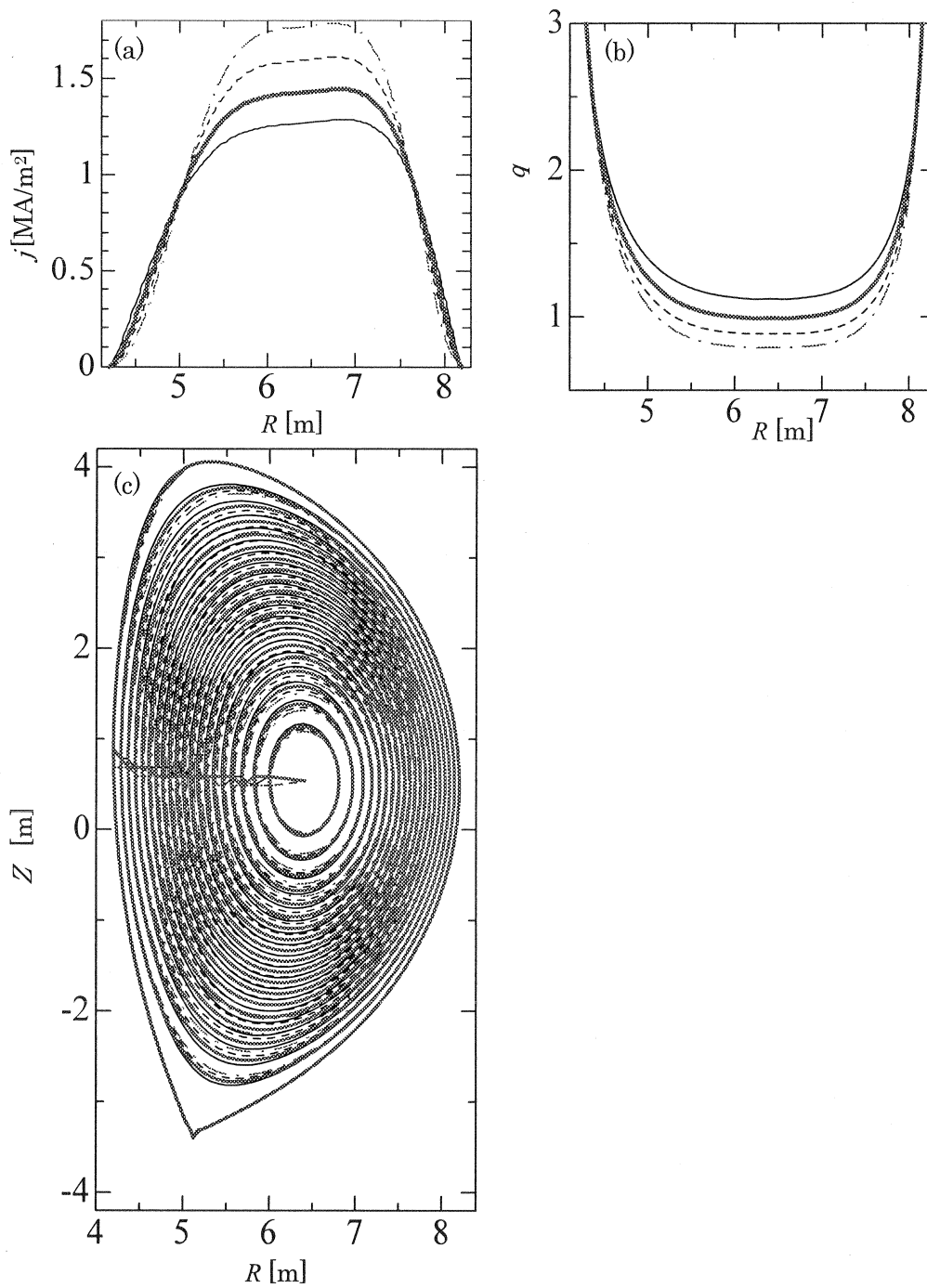


Fig. 3 The profiles of (a) the toroidal current profiles, (b) the  $q$  profiles and (c) the flux surfaces in the case of  $j_0$  scan, which are calculated by TOSCA. The bold lines show the ITER design scenario II at the start of a burn phase.

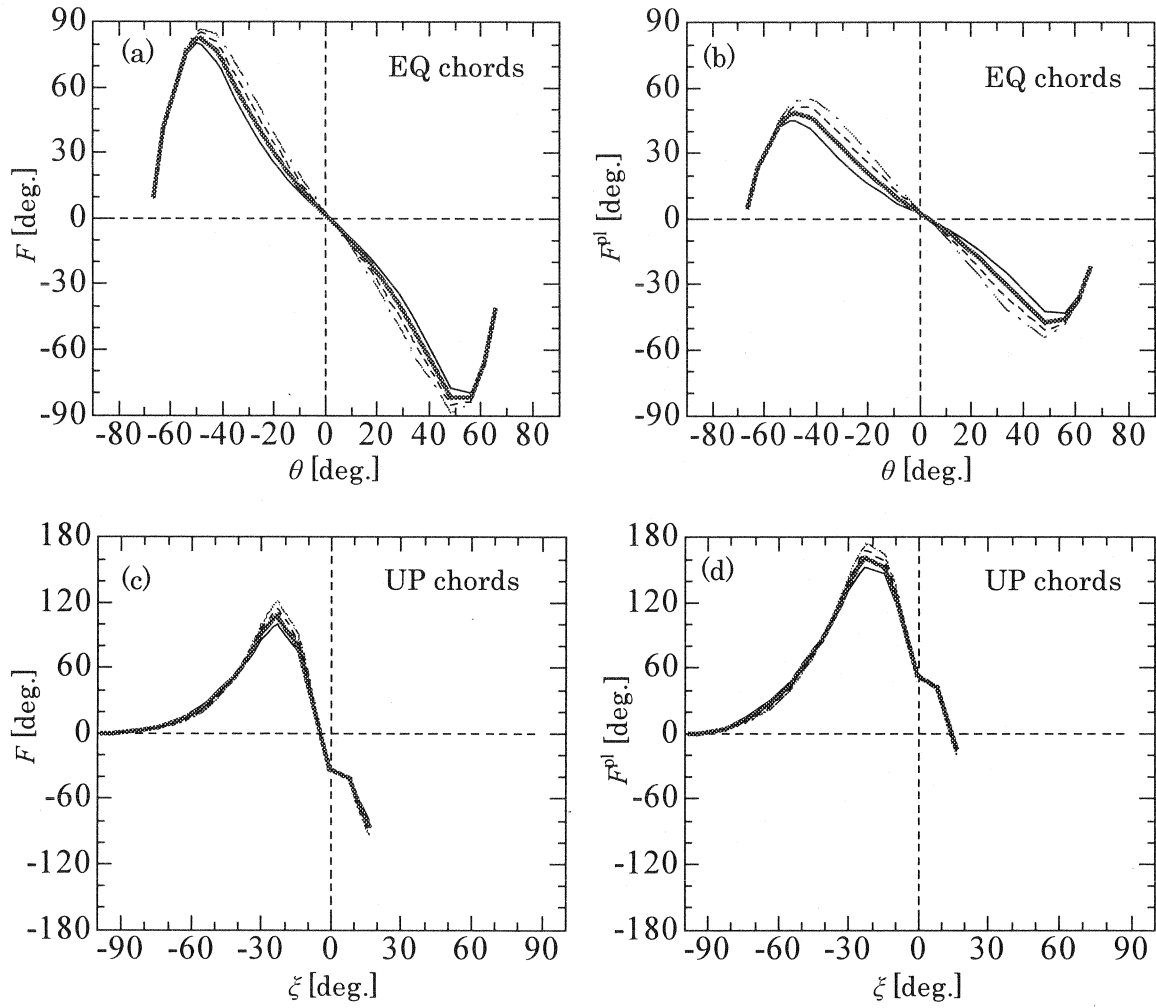


Fig. 4 Faraday rotation profiles evaluated with the sum of the toroidal current and the external field,  $F$ , ((a) and (c)) and by the toroidal current only,  $F^{pl}$ , ((b) and (d)) in the case of  $j_0$  scan. The line styles correspond to those shown in Fig. 3.

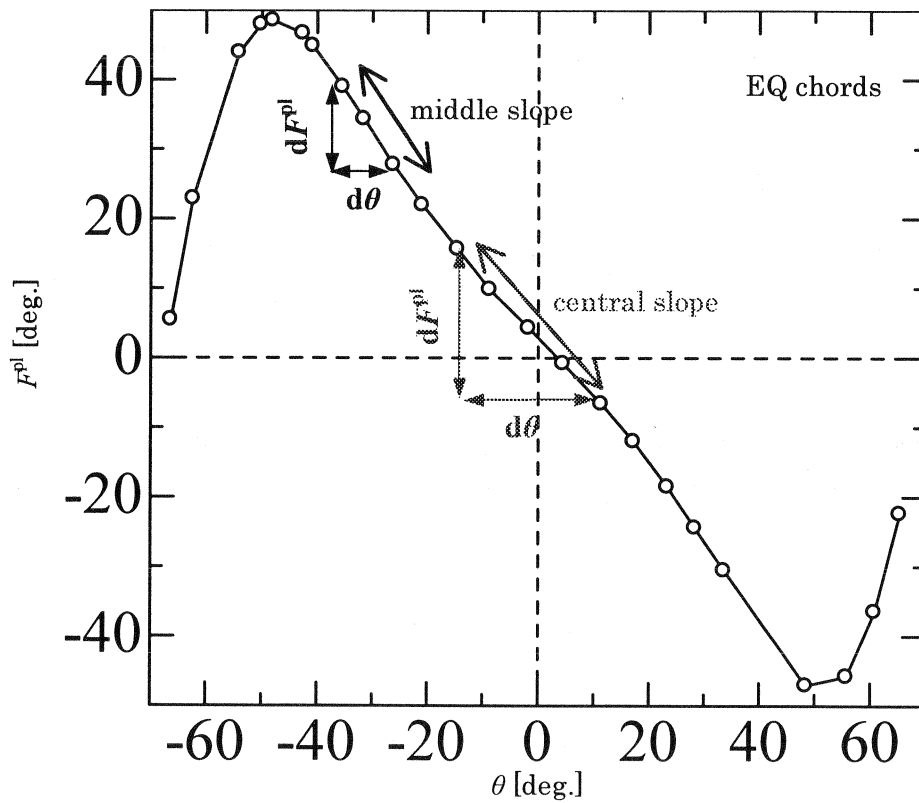


Fig. 5 The definitions of the central slope and the middle slope. Those slopes are defined by  $dF^{pl}/d\theta$ . For the central slope,  $dF^{pl}$  is a difference between  $F^{pl}$  of viewing chords of the EQ port at  $\theta = -15$  deg. and that at 11 deg.. For the middle slope,  $dF^{pl}$  is a difference between  $\theta = -35$  deg. and that at -26 deg..

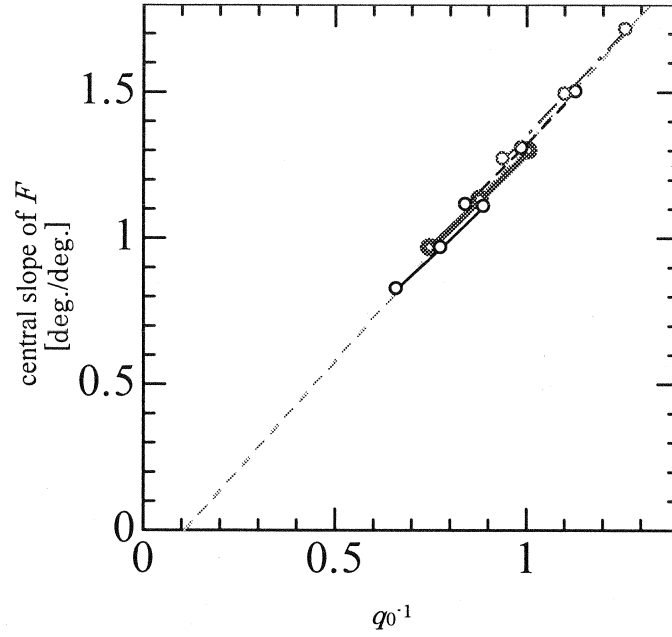


Fig. 6 The relationship between  $q_0^{-1}$  and  $F$ . Three different plasma current,  $I_p$ , (11, 13 and 15 MA) are used and other conditions are same as those for Fig.3. The line styles correspond to the current profile shape shown in Fig.3.

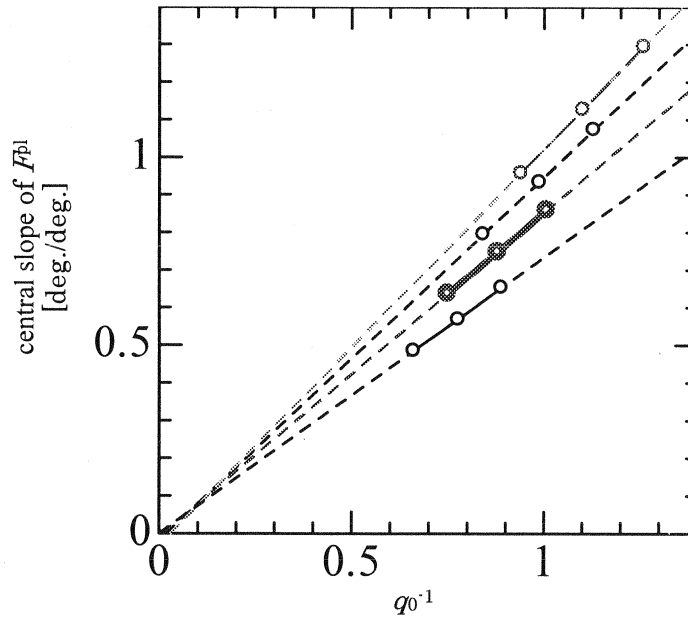


Fig. 7 The relationship between  $q_0^{-1}$  and  $F^{PL}$ . Three different plasma current,  $I_p$ , (11, 13 and 15 MA) are examined and other conditions are same as those for Fig.3. The line styles correspond to the current profile shape shown in Fig.3.

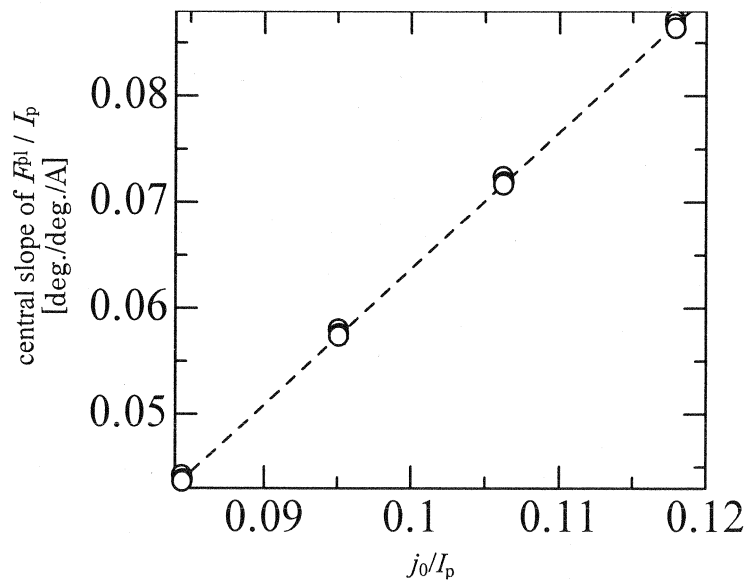


Fig. 8 The dependence of  $j_0$  on the central slope of  $F^{pl}$  in the EQ port. The calculated conditions are same as that for Fig.7.

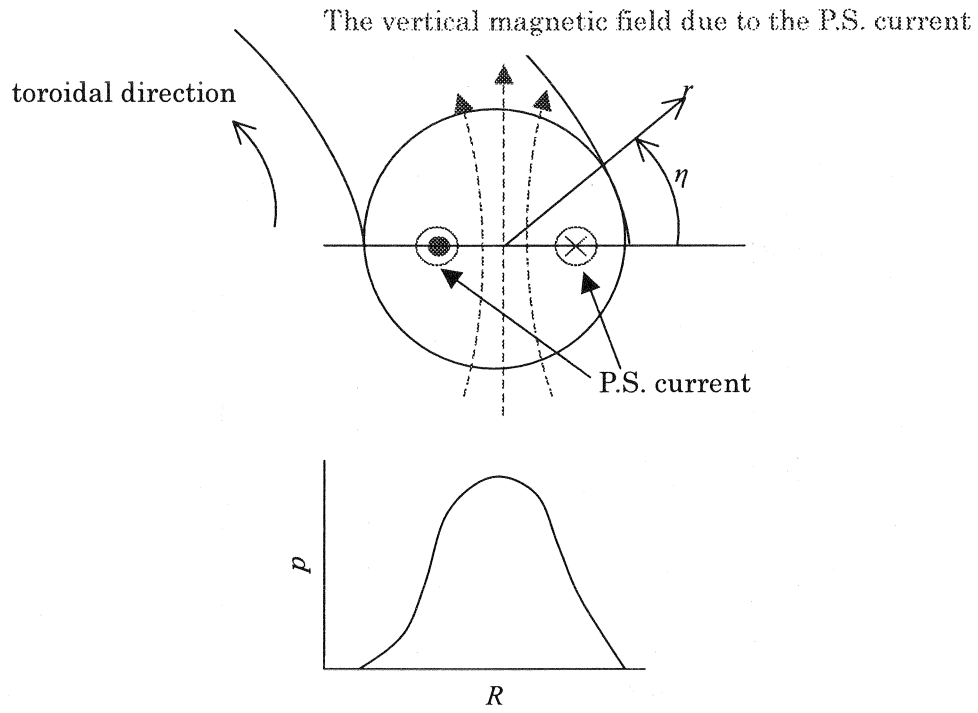


Fig. 9 The schematic illustration of the P.S. current.  $r$  shows the minor radius,  $R$  shows the major radius and  $\eta$  shows the poloidal angle.  $P$  shows the isotropic plasma pressure. The strength and the direction of the P.S. current depend on the gradient of the plasma pressure. Therefore the P.S. current has a dipole type current structure. The vertical magnetic field is induced by the dipole type current structure.

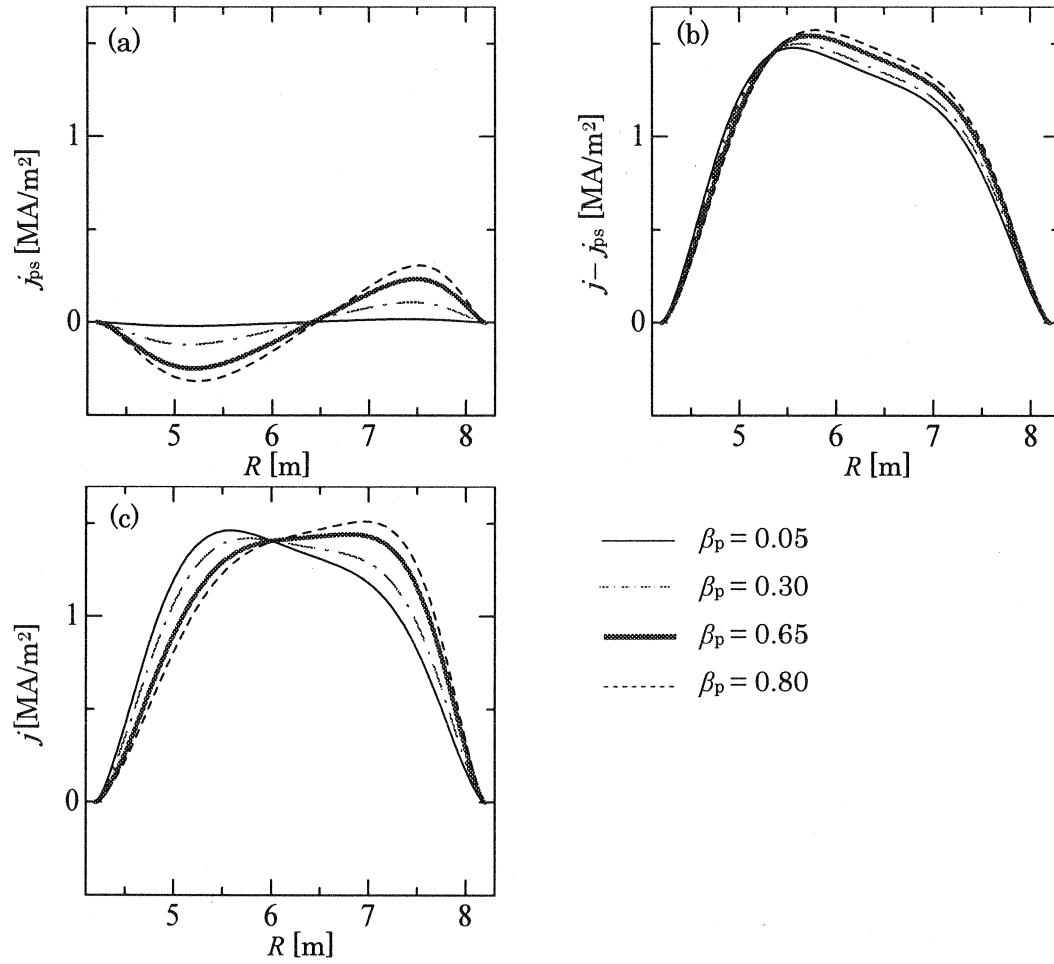


Fig. 10 The profiles of (a) the P.S. current, (b) the toroidal current without the P.S. current and (c) the toroidal current ( (a)+(b) ) in the case of  $\beta_p$  scan. The current profile without the P.S. current is fixed to investigate the effect of the P.S. current.

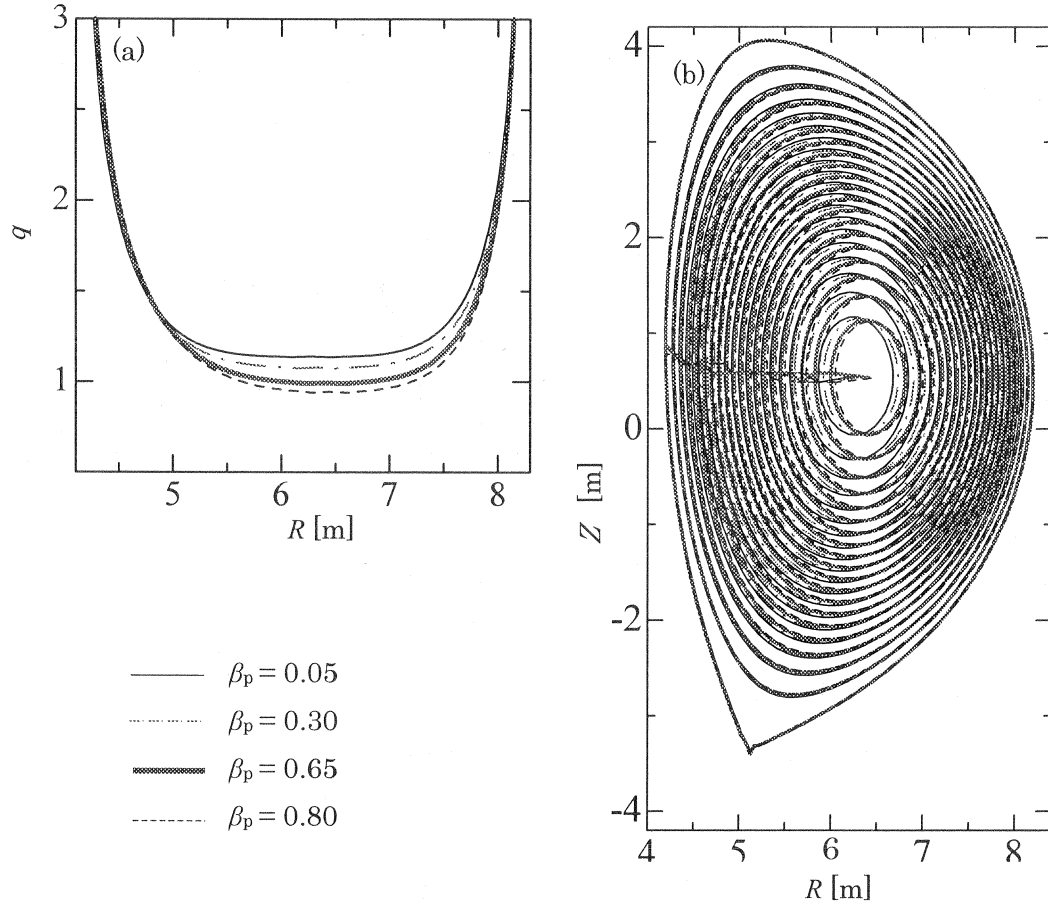


Fig. 11 (a) The  $q$  profiles and (b) the magnetic surfaces in the case of  $\beta_p$  scan.

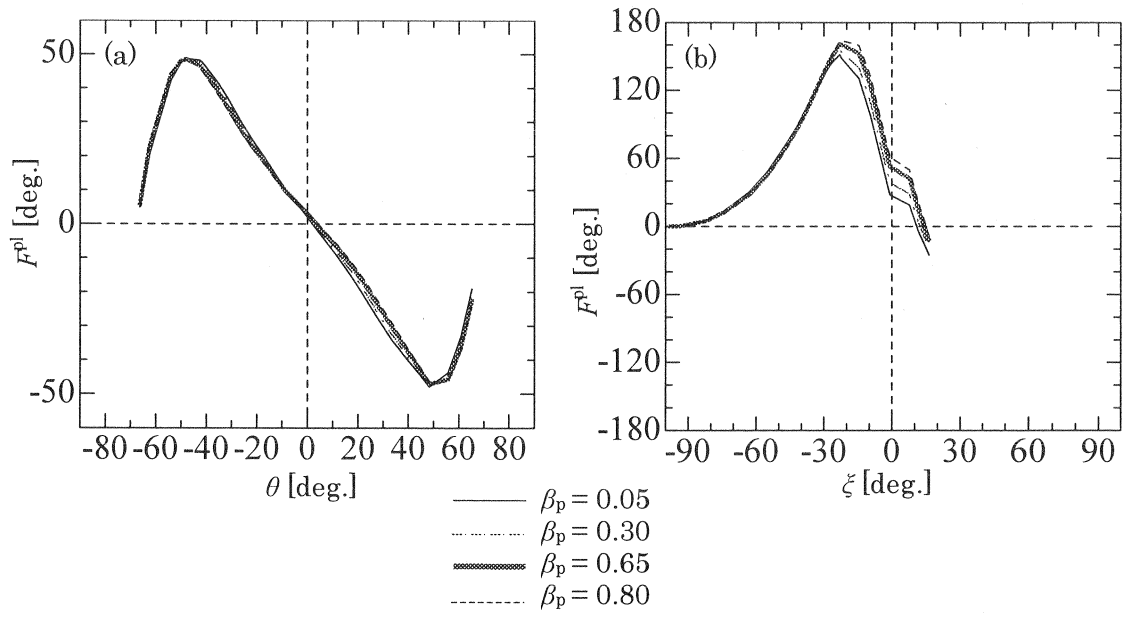


Fig. 12  $F^{\text{pl}}$  in (a) the EQ port and (b) UP port, in the case of  $\beta_p$  scan.



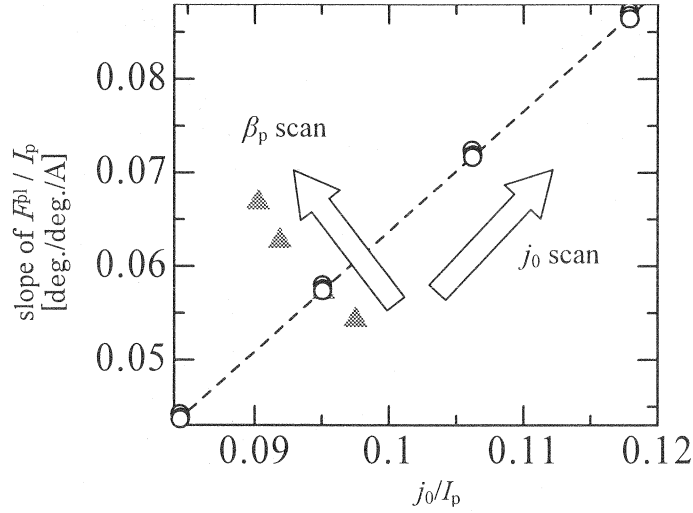


Fig. 13 The dependence of the toroidal current profile and  $\beta_p$  on the central slope of  $F^{pl}$  in the EQ port. The calculated conditions of circles are same as that for Fig. 7. The  $F^{pl}$  profiles correspond to triangles are shown in Fig. 12.

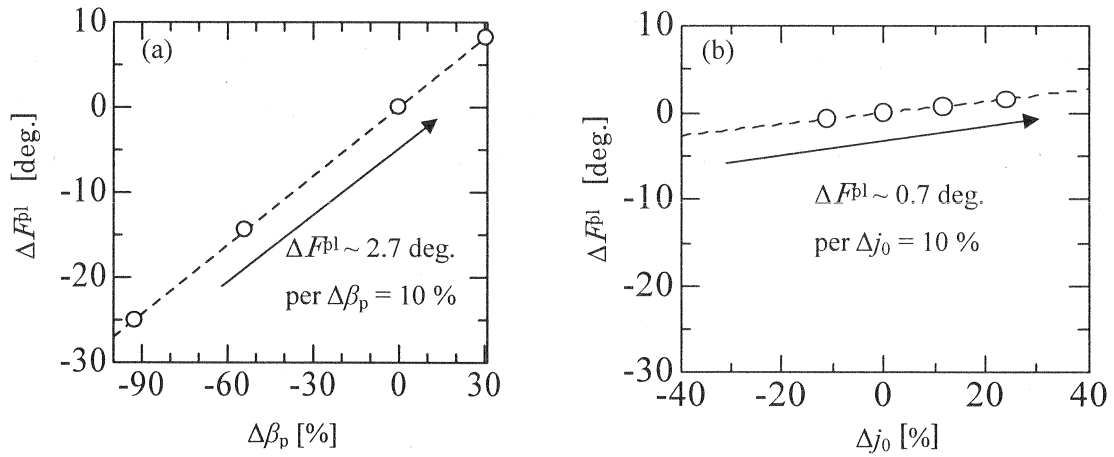


Fig. 14 The sensitivity of the central chord of the UP port to (a)  $\beta_p$  and (b)  $j_0$ .  $\Delta\beta_p$  and  $\Delta j_0$  are defined as the relative difference from those of S2-SOB. The change in  $\Delta\beta_p = 10\%$  induces 2.7 deg. of  $\Delta F^{pl}$  although the change in  $\Delta j_0 = 10\%$  induces only 0.7 deg. of  $\Delta F^{pl}$ .

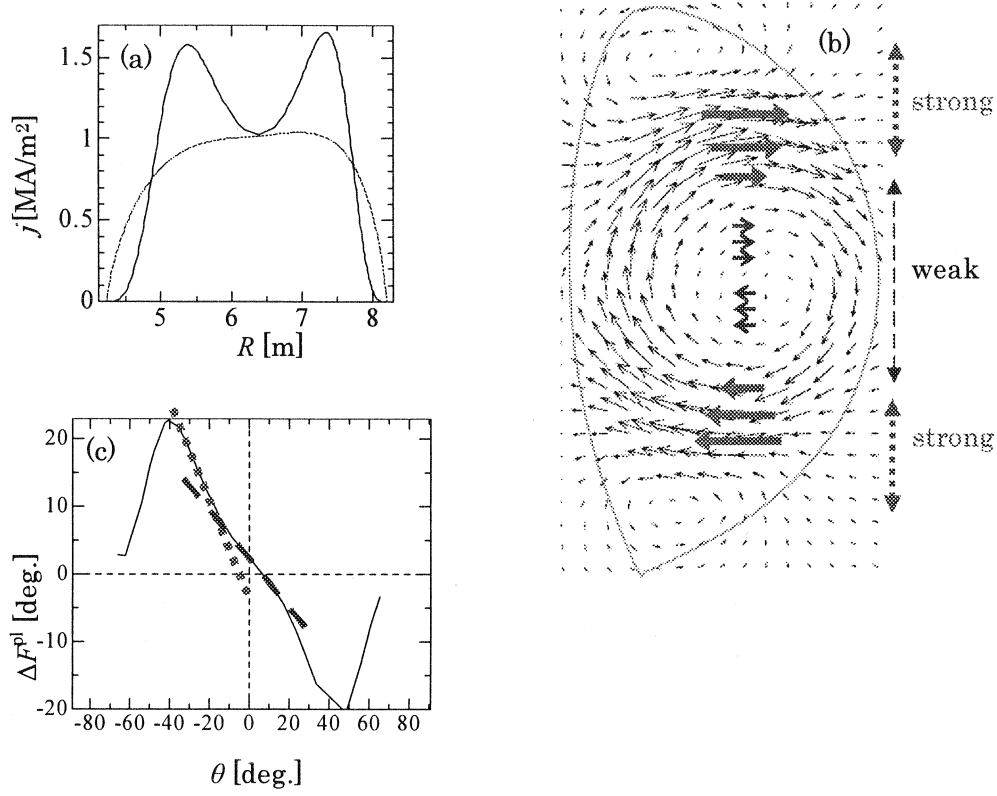


Fig. 15 (a) The toroidal current profile in the case of the normal magnetic shear and in the case of the negative magnetic shear. (b) The difference of magnetic fields due to current profiles in (a). (c) Faraday rotation due to the toroidal current only in EQ chord which are calculated by the difference of magnetic field shown in (b).

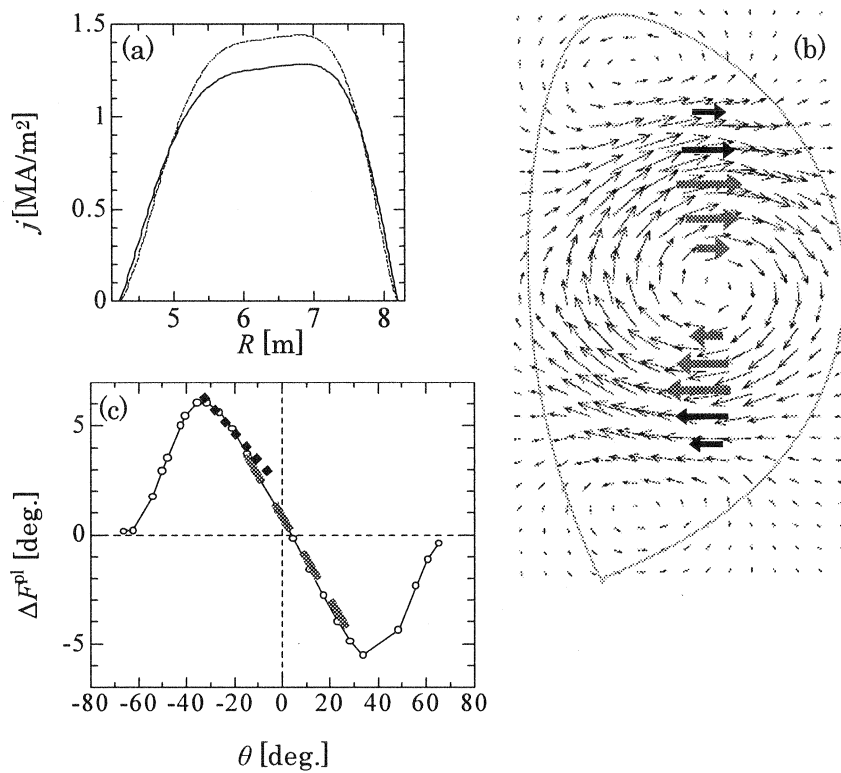


Fig. 16 (a) Two toroidal current profiles in the case of the normal magnetic shear. (b) The difference of magnetic fields due to current profiles in (a). (c) Faraday rotation due to the toroidal current only in EQ chord which are calculated by the difference of magnetic field shown in (b).

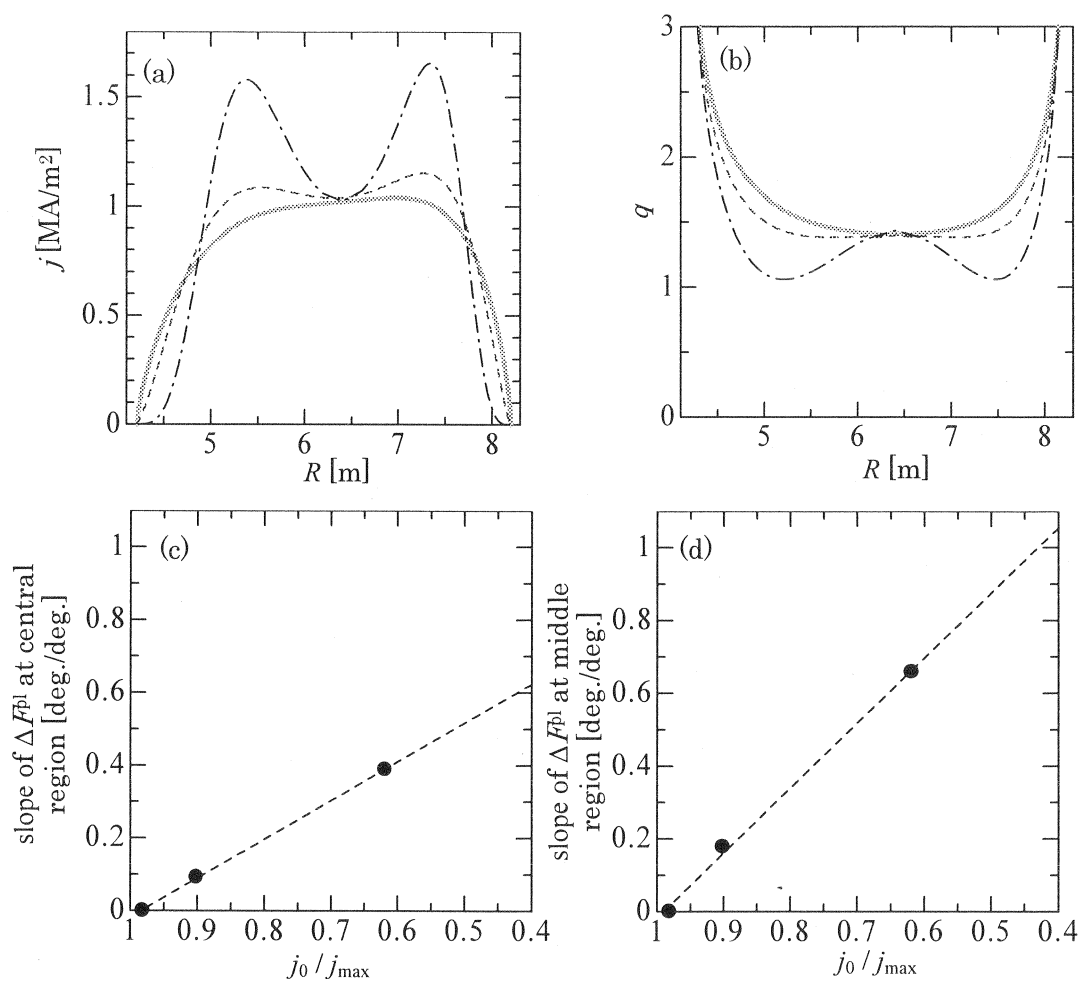


Fig. 17 The sensitivities of  $j_0/j_{\text{max}}$ . (a) Toroidal current profiles, (b)  $q$  profiles, (c) the slope of  $\Delta F^{\text{pl}}$  at the central viewing chords in the EQ port and (d) the slope of  $\Delta F^{\text{pl}}$  at the middle viewing chords in the EQ port

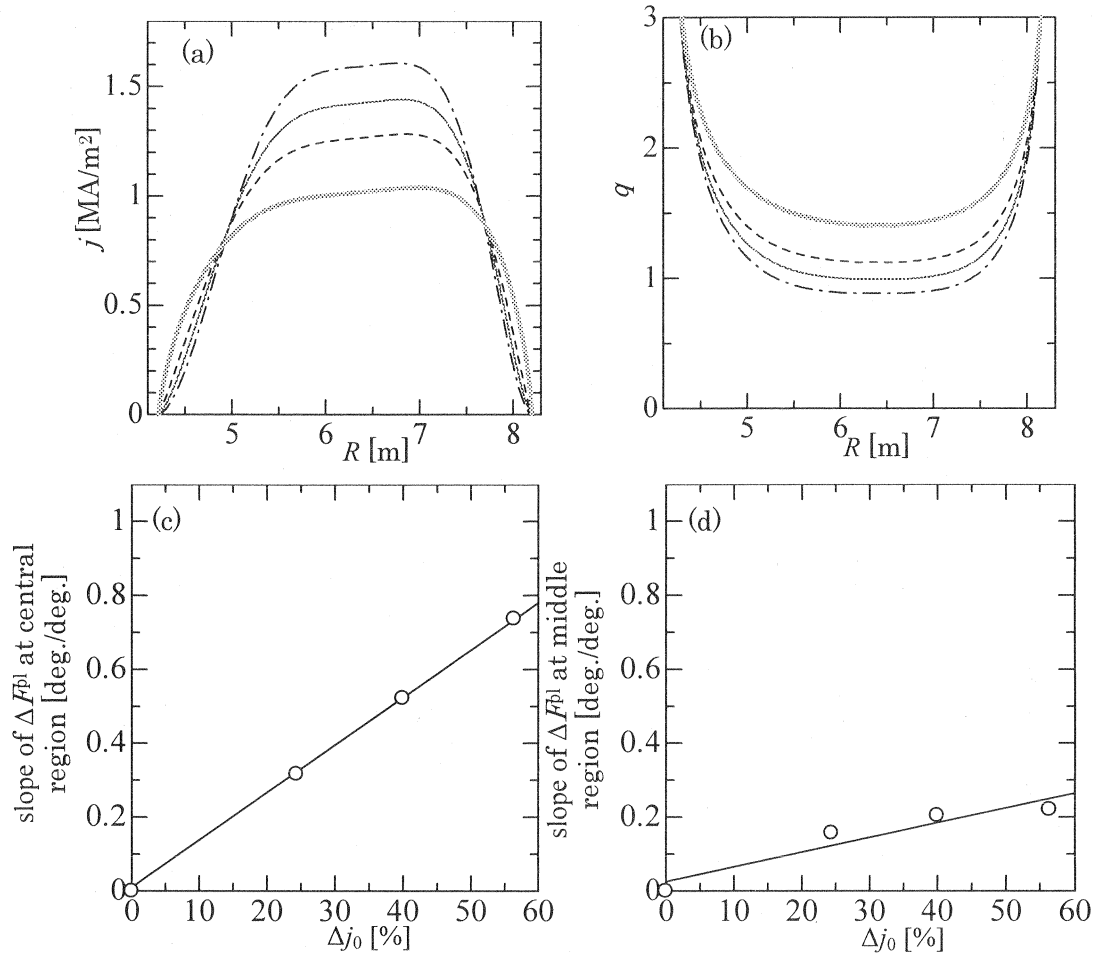


Fig. 18 The sensitivities of  $j_0$ . (a) Toroidal current profiles, (b)  $q$  profiles, (c) the slope of  $\Delta F^{\text{pl}}$  at the central viewing chords in the EQ port and (d) the slope of  $\Delta F^{\text{pl}}$  at the middle viewing chords in the EQ port

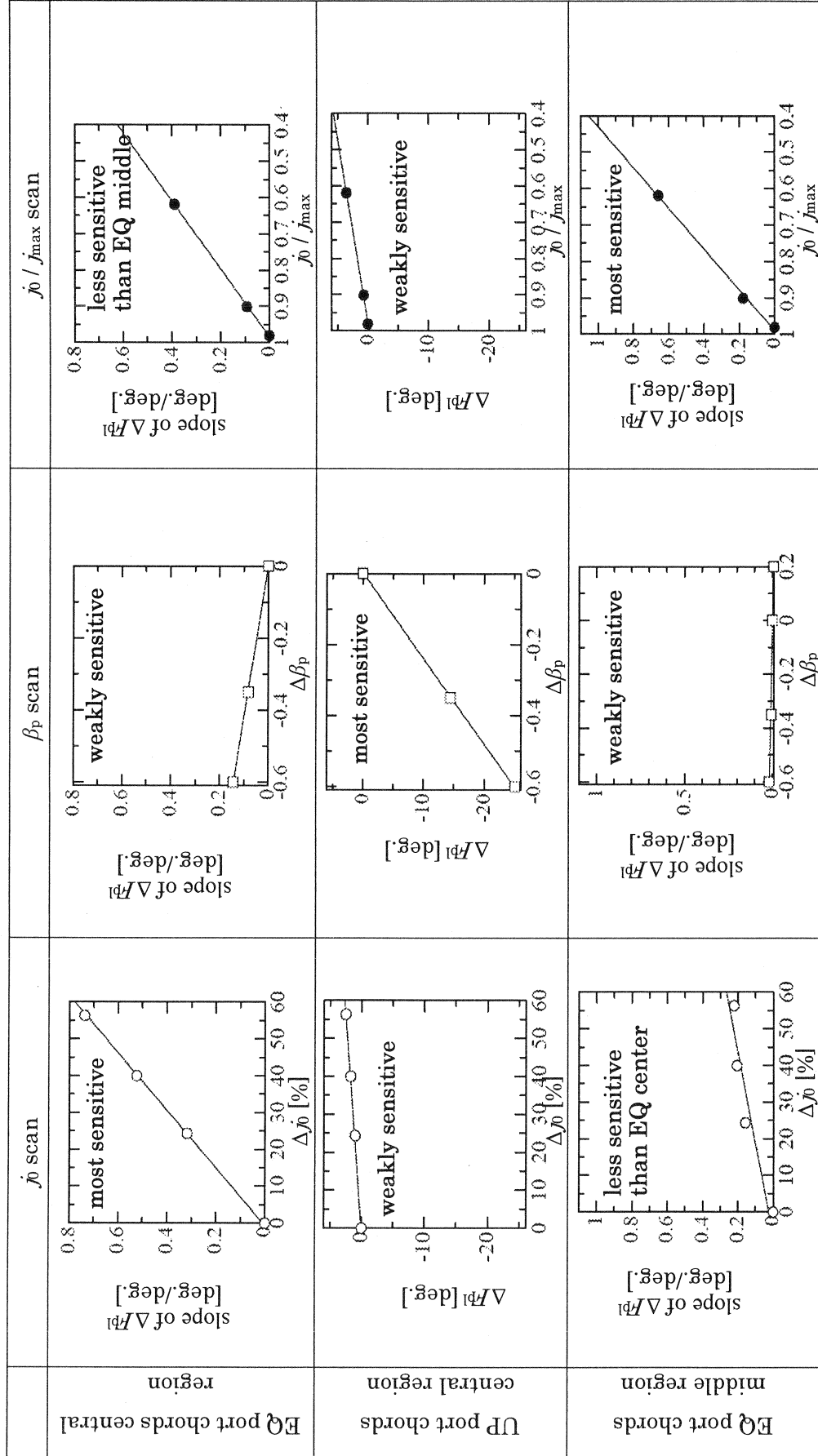


Fig. 19 The sensitivities between the current profiles and the viewing chords regions. The current profiles are scanned by changing parameters  $j_0$ ,  $\beta_p$  and  $j_0 / j_{\max}$ . Note that other conditions are fixed when one parameter is scanned. The Y-axis scale is same in graphs for one scan. Therefore the sensitivities on the each plasma parameter can be shown as the gradient of lines in graphs.

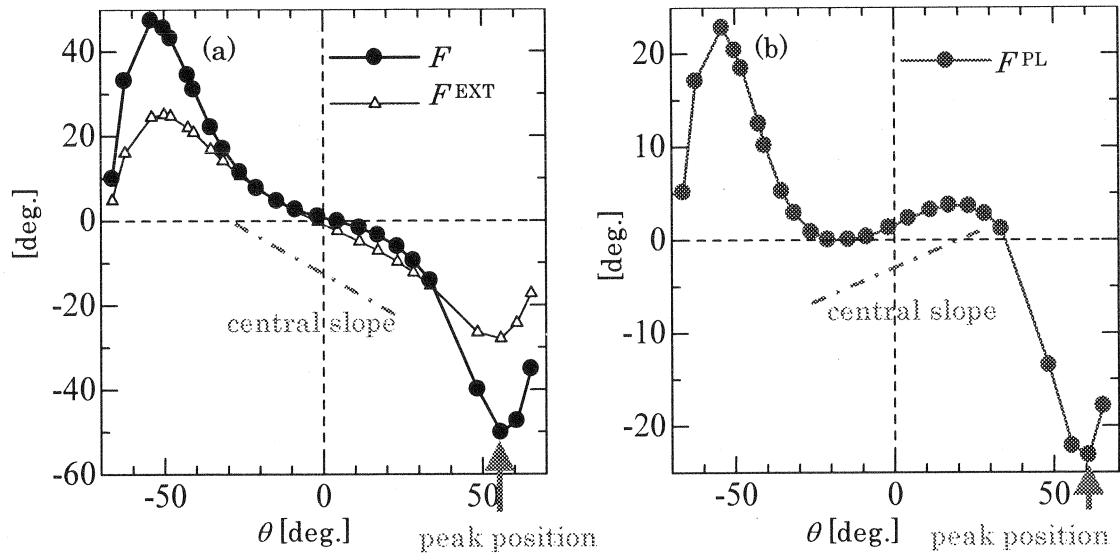


Fig. 20 (a) The profiles of  $F$  and  $F^{\text{EXT}}$  and (b) the  $F^{\text{PL}}$  profile for the non-inductive operation scenario at the start of the burn phase. The profile shapes of  $F$  and  $F^{\text{PL}}$  are different, for example, the central slopes of  $F$  and  $F^{\text{PL}}$  are much different. The peak positions of  $F$  and  $F^{\text{PL}}$  are also different.

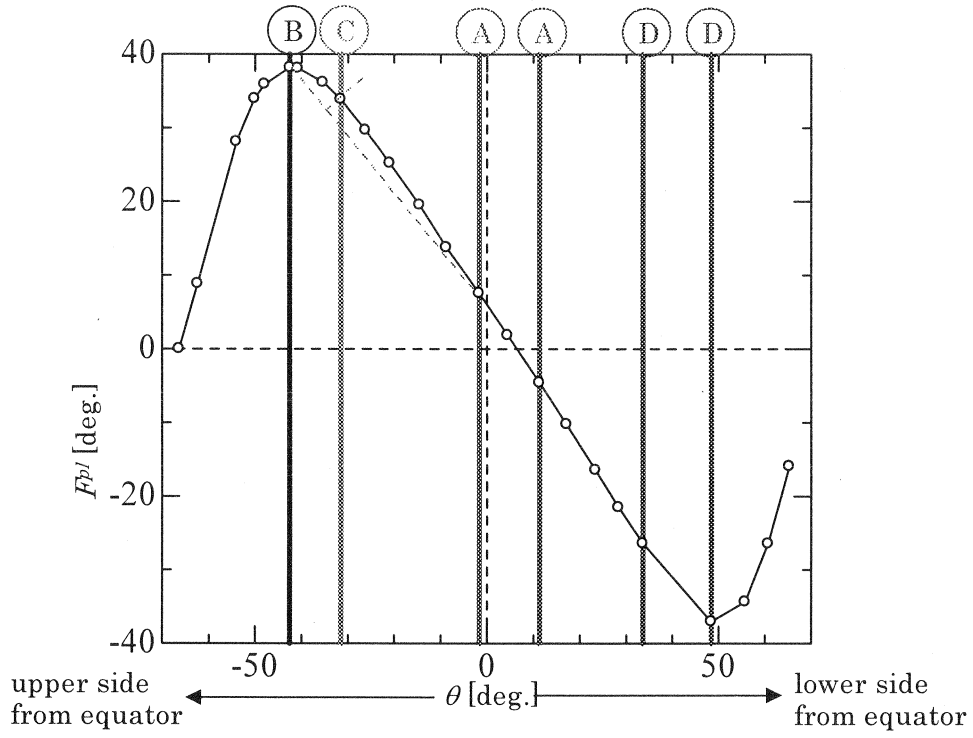


Fig. 21 The  $F^{pl}$  profile for the inductive operation scenario at  $I_p=11.5\text{MA}$ . The vertical bold lines show the viewing chord positions which are selected.

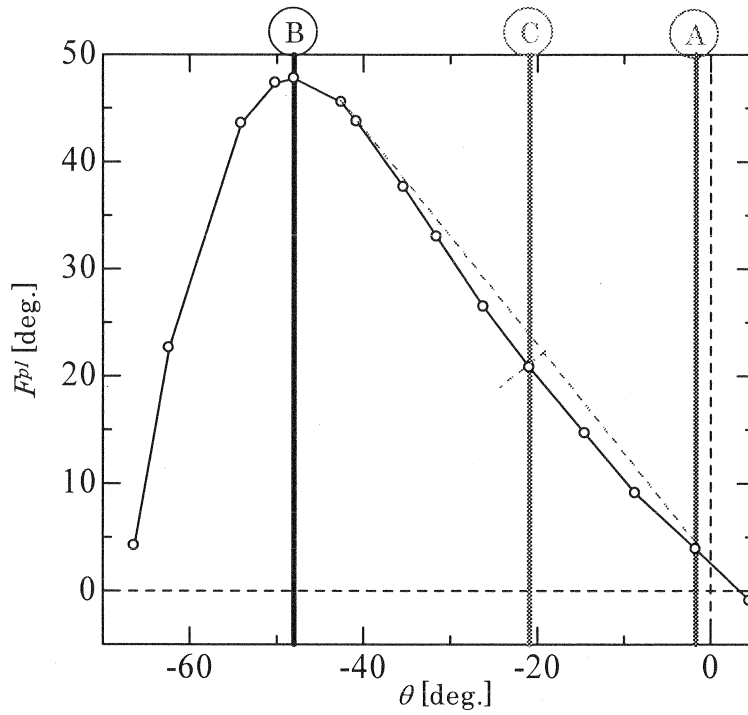


Fig. 22 The  $F^{pl}$  profile for the inductive operation scenario at  $I_p=15.0\text{MA}$ . The vertical bold lines show the viewing chord positions which are selected.



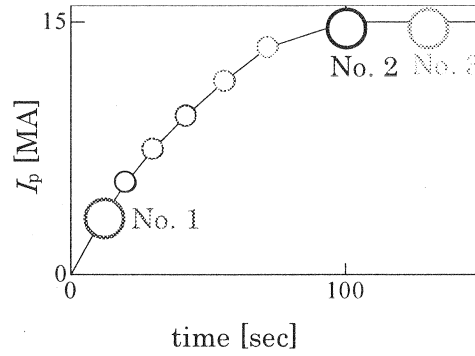


Fig. 23 The time evolution of  $I_p$  in the case of the inductive scenario II.

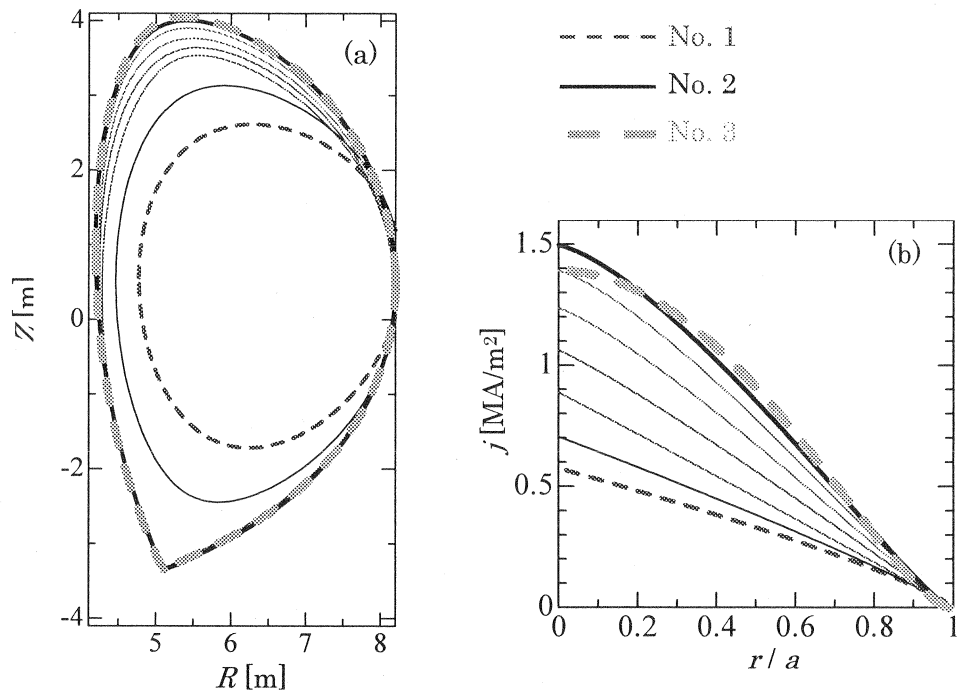


Fig. 24 (a) The LCFS and (b) the current profiles in the case of the inductive scenario II. Each number corresponds to the number in Fig. 23.

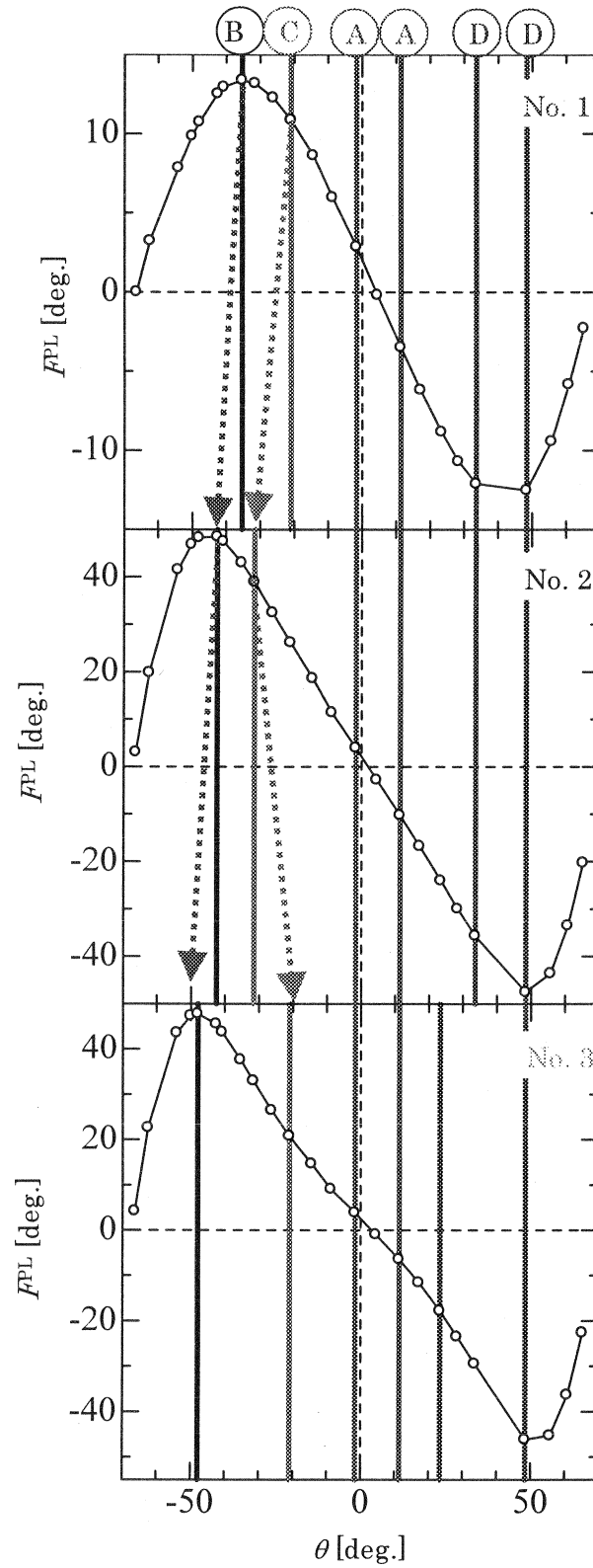


Fig. 25 The  $F^{PL}$  profiles in the case of the inductive scenario II. The vertical lines mean the selected viewing chord positions. Each number corresponds to the number in Fig. 23.

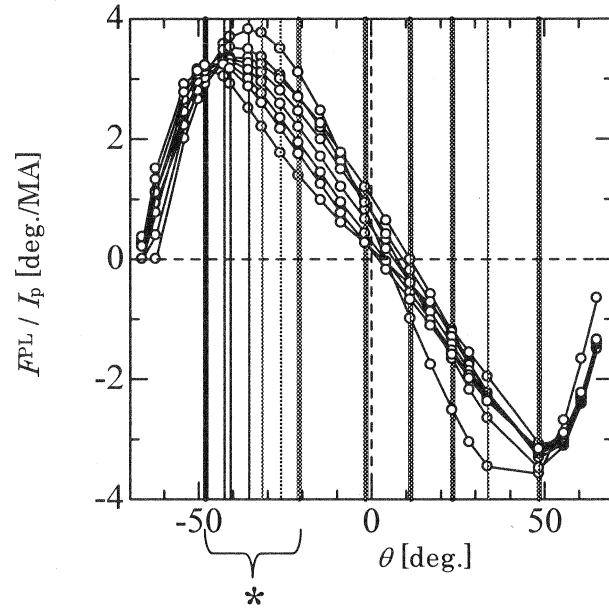


Fig. 26 The  $F^{\text{PL}}$  profiles in the case of the inductive scenario II. The vertical lines mean the selected viewing chord positions at each time. The bold vertical lines show the selected viewing chord positions at the burning phase. The region, where the remaining channels should be arranged, is shown with a symbol ‘\*’.

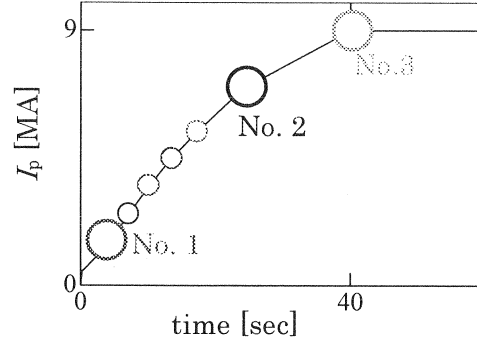


Fig. 27 The time evolution of the  $I_p$  in the case of the non-inductive scenario.

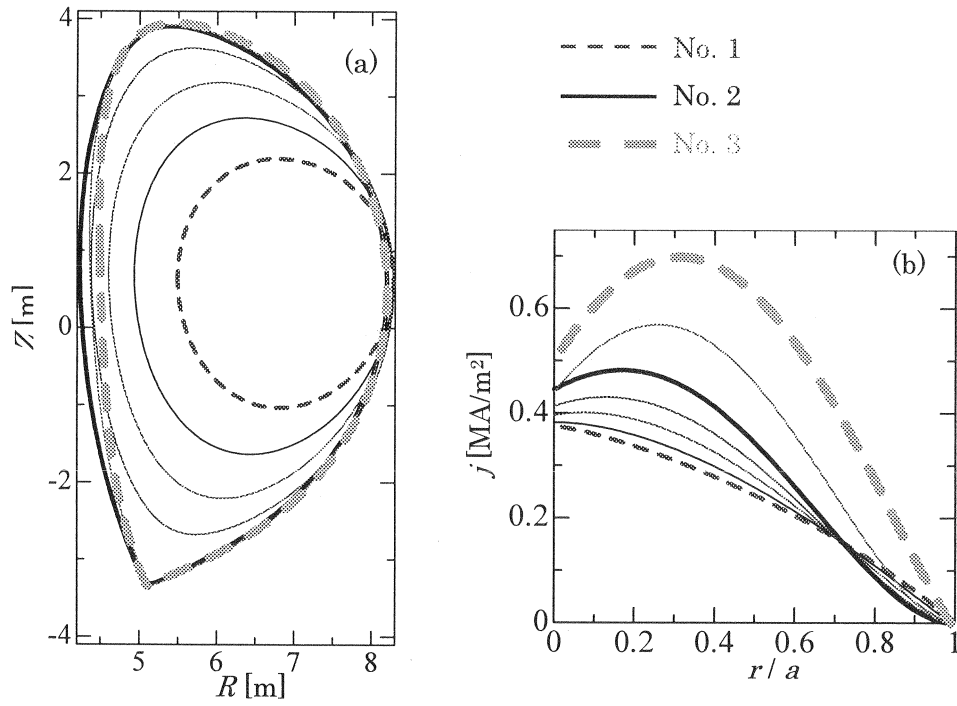


Fig. 28 (a)The LCFS and (b) the current profiles in the case of the non-inductive scenario. Each number corresponds to the number in Fig. 23.

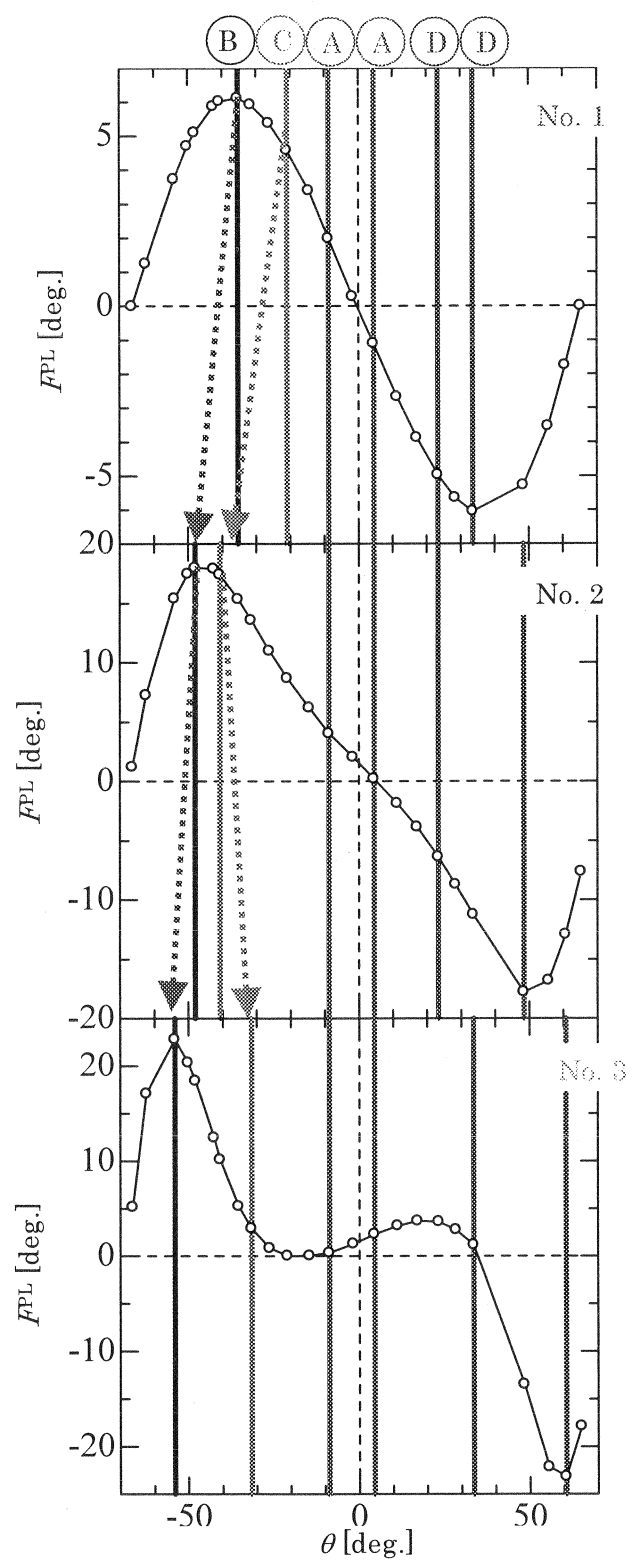


Fig. 29 The  $F^{PL}$  profiles in the case of the non-inductive scenario. The vertical lines mean the selected viewing chord positions. Each number corresponds to the number in Fig. 23.

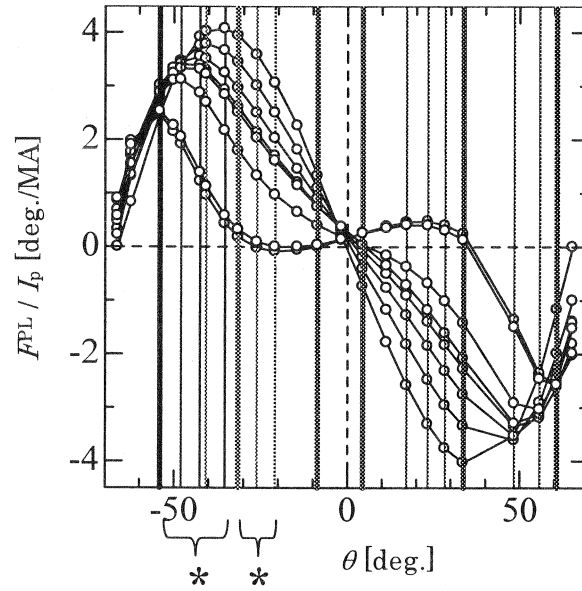


Fig. 30 The  $F^{\text{PL}}$  profiles in the case of the non-inductive scenario. The vertical lines mean the selected viewing chord positions at each time. The bold vertical lines show the selected viewing chord positions at the burning phase. The region, where the remaining channels should be arranged, is shown with a symbol ‘\*’.

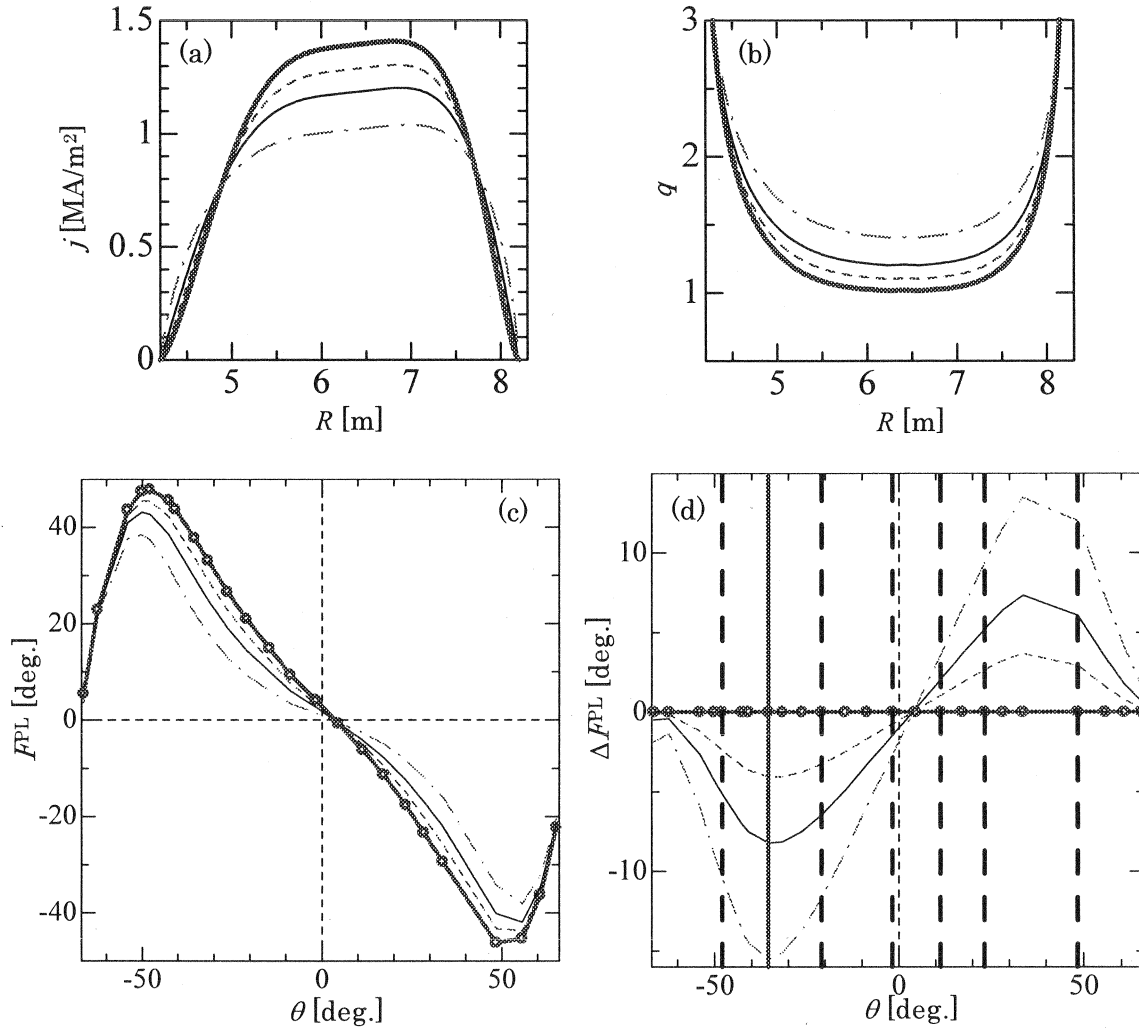


Fig. 31 The current profile scan based on the inductive operation scenario II. (a) toroidal current profiles, (b) the  $q$  profiles, (c)  $F^{\text{pl}}$  profiles and (d)  $\Delta F^{\text{pl}}$  profiles for viewing chords in the EQ port with adequate channels to detect the current profile of the operation scenario (vertical bold broken lines) and the adequate channel to detect the change in the current profile (vertical bold line).

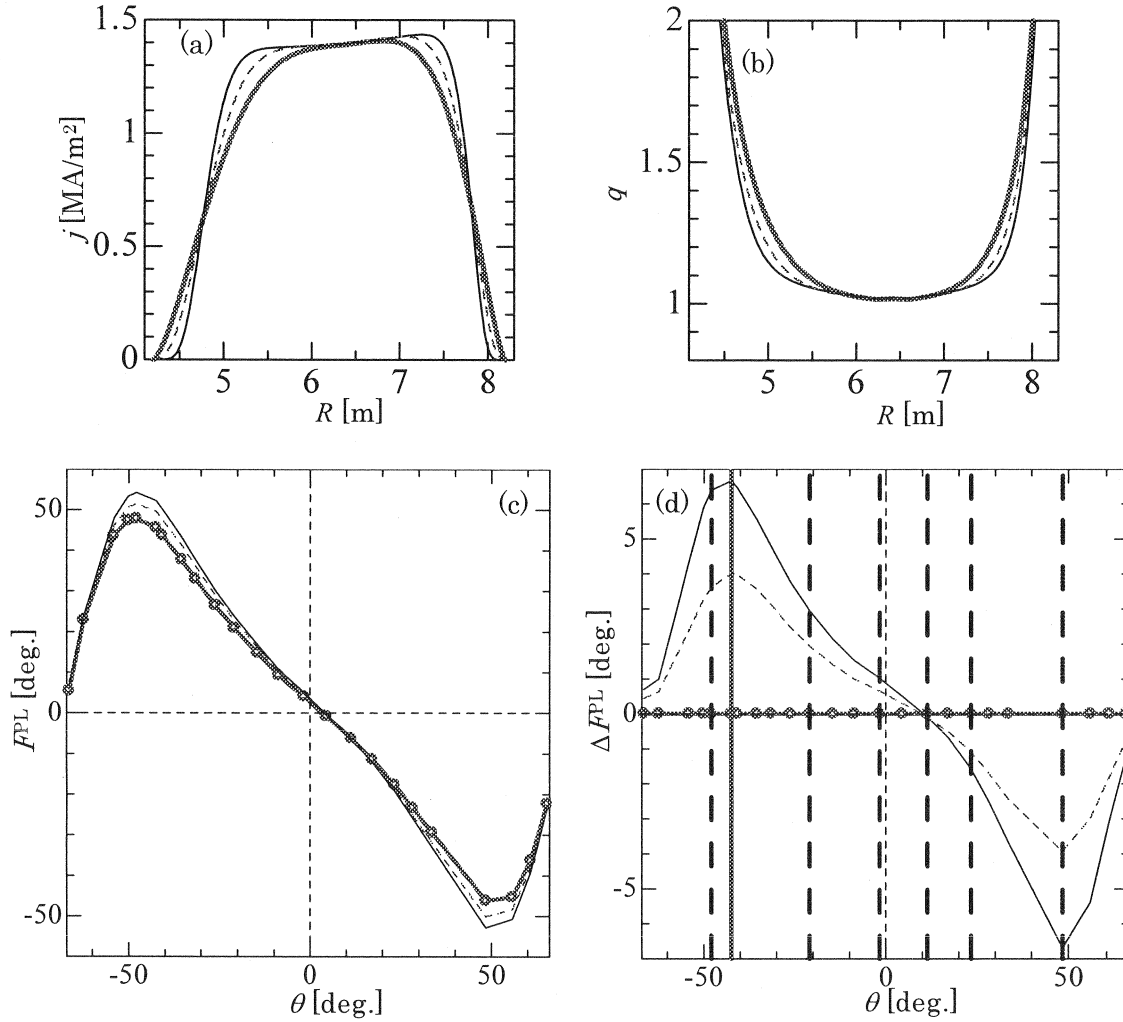


Fig. 32 The current profile scan based on the inductive operation scenario II. (a) Toroidal current profiles, (b) the  $q$  profiles, (c)  $F^{\text{pl}}$  profiles and (d)  $\Delta F^{\text{pl}}$  profiles for viewing chords in the EQ port with adequate channels to detect the current profile of the operation scenario (vertical bold broken lines) and the adequate channel to detect the change in the current profile (vertical bold line).



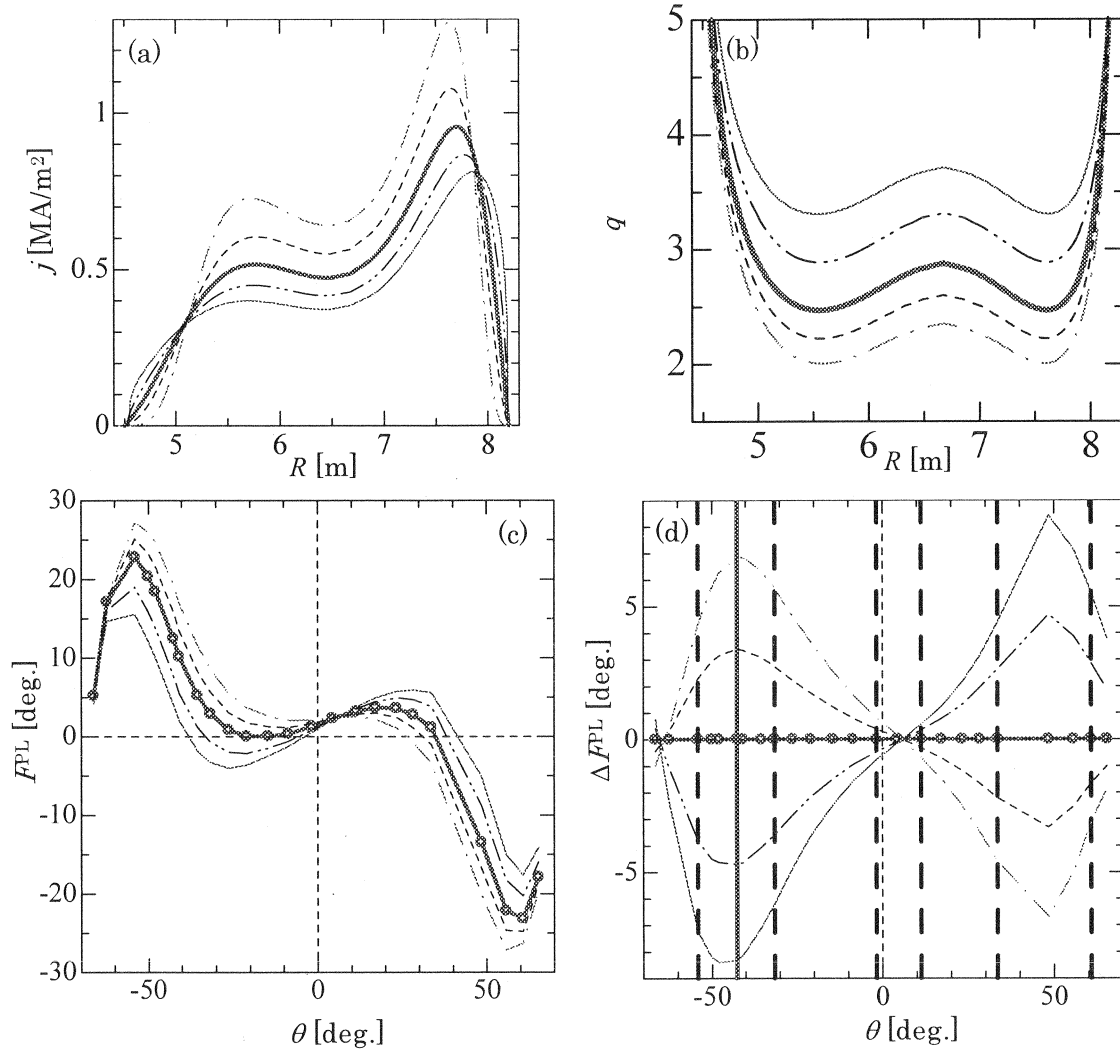


Fig. 33 The current profile scan based on the inductive operation scenario II. (a) Toroidal current profiles, (b) the  $q$  profiles, (c)  $F^{\text{pl}}$  profiles and (d)  $\Delta F^{\text{pl}}$  profiles for viewing chords in the EQ port with adequate channels to detect the current profile of the operation scenario (vertical bold broken lines) and the adequate channel to detect the change in the current profile (vertical bold line).

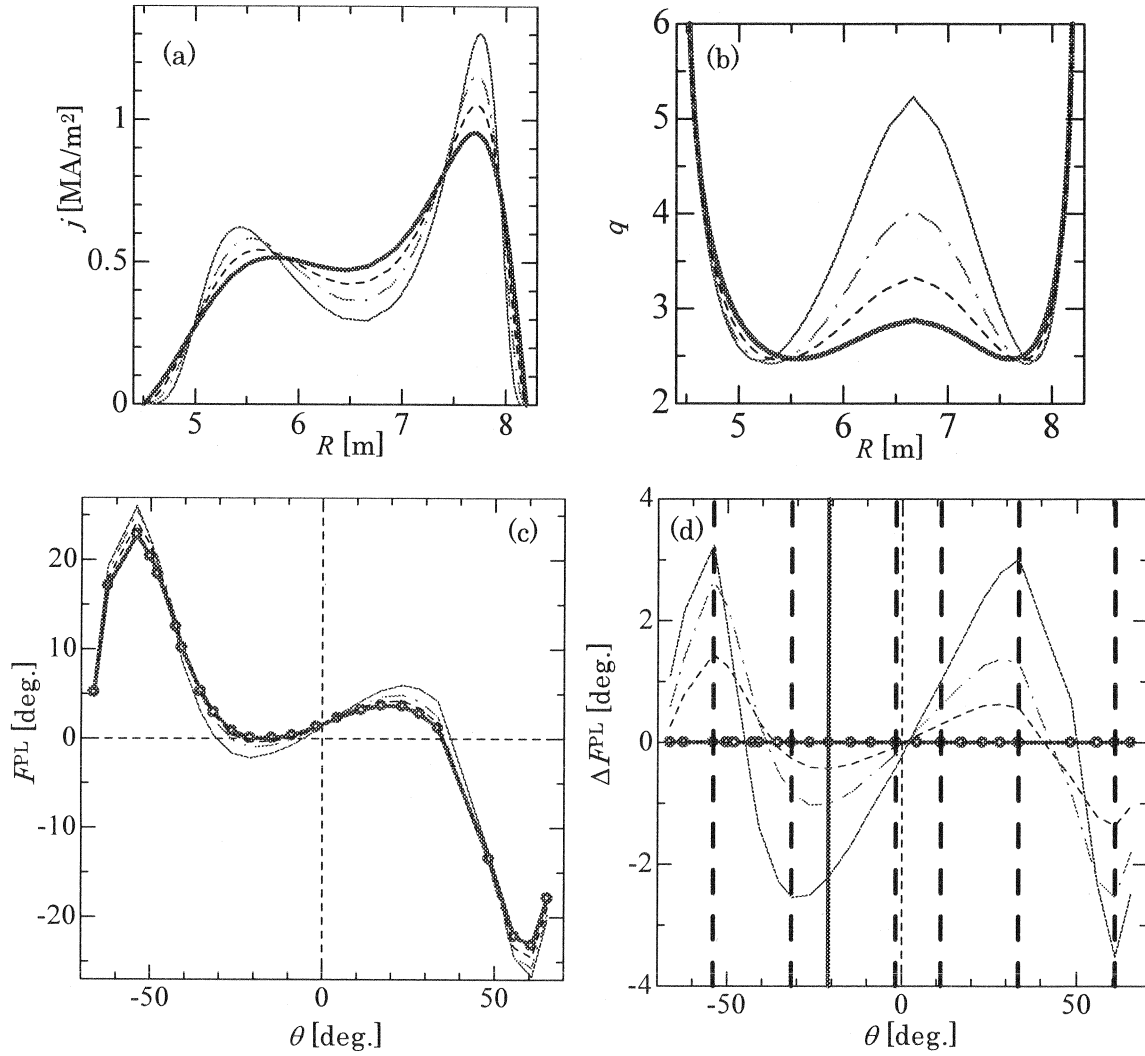


Fig. 34 The current profile scan based on the inductive operation scenario II. (a) Toroidal current profiles, (b) the  $q$  profiles, (c)  $F^{pl}$  profiles and (d)  $\Delta F^{pl}$  profiles for the EQ port with adequate channels to detect the current profile of the operation scenario (vertical bold broken lines) and the adequate channel to detect the change in the current profile (vertical bold line).

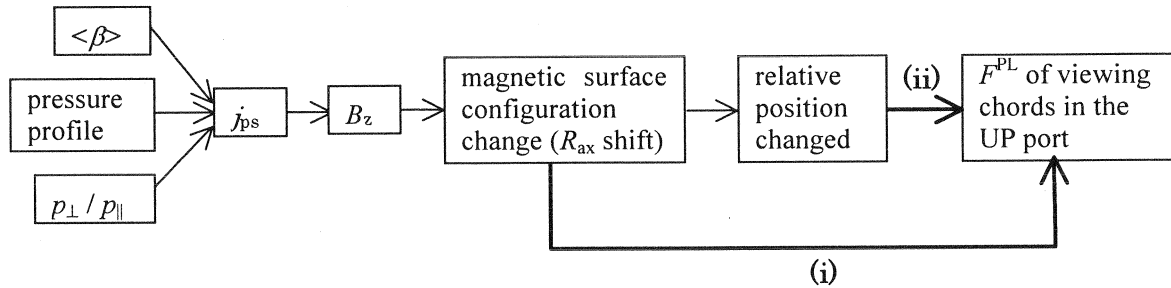


Fig. 35 The mechanism of the finite  $\beta$  effect on the  $F^{pl}$  of viewing chords in the UP port. The P.S. current depends on the average beta, the pressure profile and the pressure anisotropy. The P.S. current induces the vertical magnetic field,  $B_z$ . The magnetic axis position,  $R_{ax}$ , is shifted by the  $B_z$ . (i) The vertical magnetic field due to the P.S. current affects directly the central viewing chord in the UP port (see also Fig. 36), and (ii) the relative position between the viewing chord and the magnetic axis are changed by the Shafranov shift (see also Fig. 36).

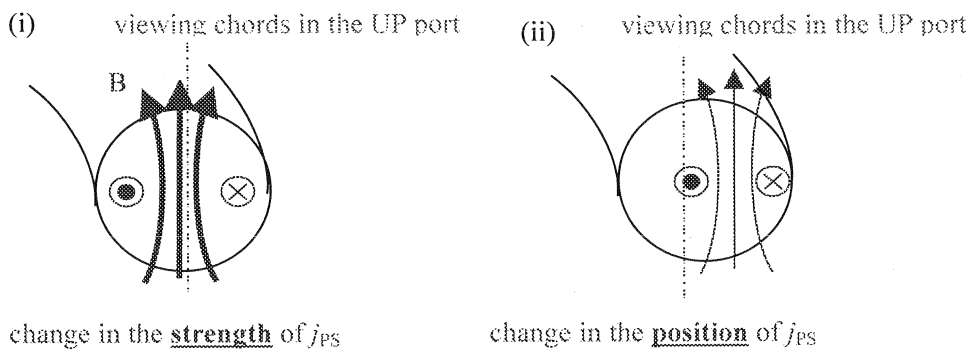


Fig. 36 The mechanism of the finite  $\beta$  effect on the  $F^{pl}$  of viewing chords in the UP port. (i) The vertical magnetic field due to the P.S. current affects directly the central viewing chord in the UP port (see also “(i)” in Fig. 35) and (ii) the relative position between the viewing chord and the magnetic axis are changed by the Shafranov shift (see also “(ii)” in Fig. 35).

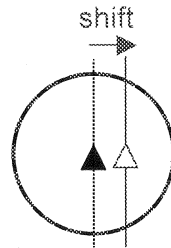
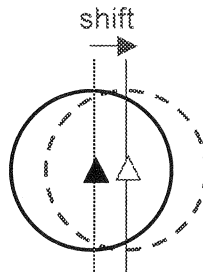
(a) the  $R_{ax}$  shift by the finite beta effect(b) the  $R_{ax}$  shift by the change in external coil currents

Fig. 37 The schematic illustrations of (i) the  $R_{ax}$  shift by the finite beta effect and (ii) the  $R_{ax}$  shift by the change in external coil currents. The bold circles show the LCFS before the  $R_{ax}$  shift. The broken circles show the LCFS after the  $R_{ax}$  shift. The closed triangles and the open triangles show the  $R_{ax}$  position before and after the shift, respectively.

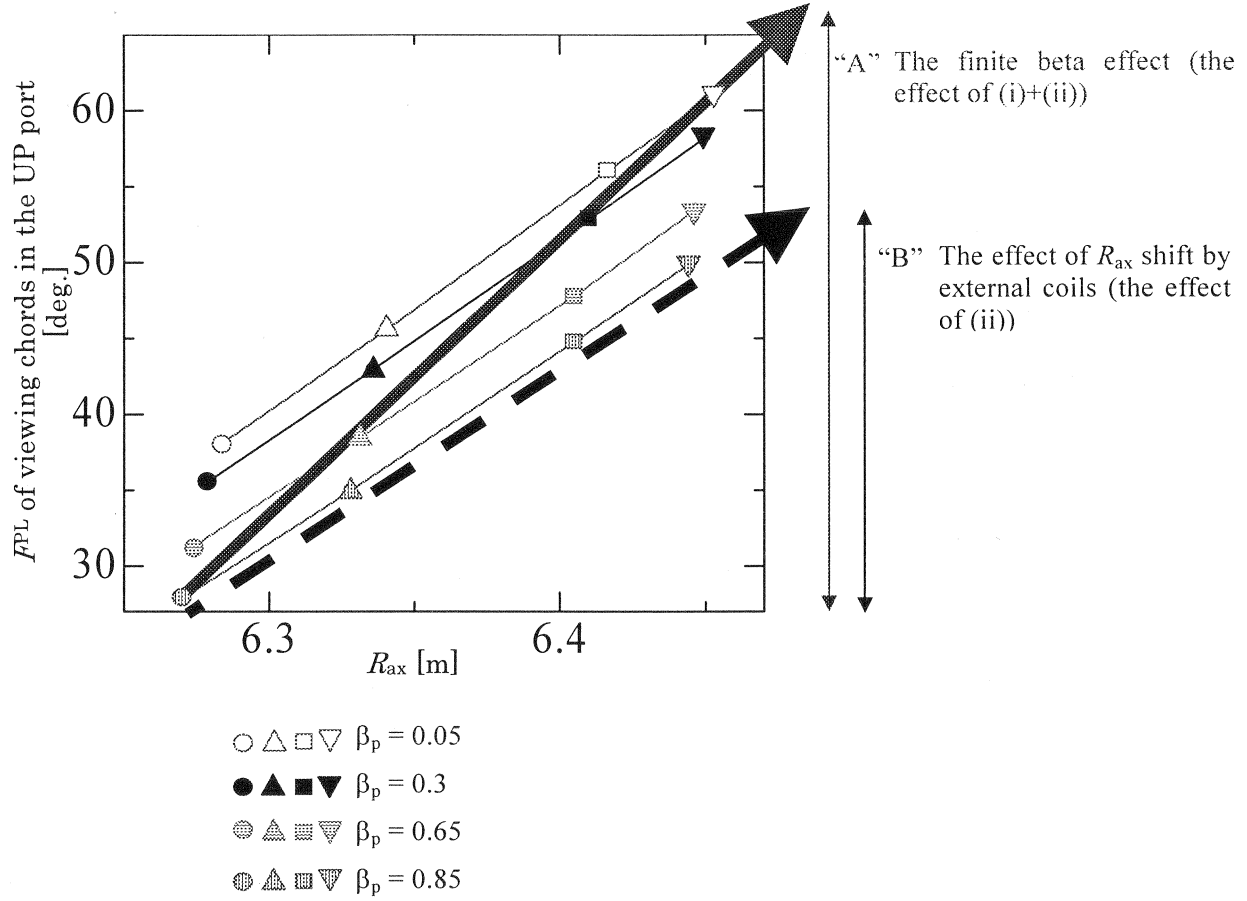


Fig. 38 The relationship between  $R_{\text{ax}}$  and  $F^{\text{pl}}$ , where  $R_{\text{ax}}$  shift is induced by the external coils or the finite beta effect. The painted patterns mean the difference of  $\beta_p$  and the shapes of symbols show the difference of  $R_{\text{ax}}$  shift by external coils. The change in  $\Delta\beta_p = 0.1$  induces  $\Delta F^{\text{pl}} \approx 4$  deg., i.e. it is the effect of (i) and (ii), and  $\Delta R_{\text{ax}} \approx 0.02$  m (see "A"). The change in  $F^{\text{pl}}$  is about 3 deg. if  $\Delta R_{\text{ax}} \approx 0.02$  m is induced by external coil's current, i.e. it is assumed as the effect of (ii) (see "B").

This is a blank page.

# 国際単位系（SI）

表 1. SI 基本単位

基本量	SI 基本単位	
	名称	記号
長さ	メートル	m
質量	キログラム	kg
時間	秒	s
電流	アンペア	A
熱力学温度	ケルビン	K
物質量	モル	mol
光度	カンデラ	cd

表 2. 基本単位を用いて表されるSI組立単位の例

組立量	SI 基本単位	
	名称	記号
面積	平方メートル	m <sup>2</sup>
体積	立方メートル	m <sup>3</sup>
速度	メートル毎秒	m/s
加速度	メートル毎秒毎秒	m/s <sup>2</sup>
波数	毎メートル	m <sup>-1</sup>
密度（質量密度）	キログラム毎立方メートル	kg/m <sup>3</sup>
質量体積（比体積）	立法メートル毎キログラム	m <sup>3</sup> /kg
電流密度	アンペア毎平方メートル	A/m <sup>2</sup>
磁界の強さ	アンペア毎メートル	A/m
（物質量の）濃度	モル毎立方メートル	mol/m <sup>3</sup>
輝度	カンデラ毎平方メートル	cd/m <sup>2</sup>
屈折率	（数の）1	1

表 5. SI 接頭語

乗数	接頭語	記号	乗数	接頭語	記号
10 <sup>24</sup>	ヨタ	Y	10 <sup>-1</sup>	デシ	d
10 <sup>21</sup>	ゼタ	Z	10 <sup>-2</sup>	センチ	c
10 <sup>18</sup>	エクサ	E	10 <sup>-3</sup>	ミリ	m
10 <sup>15</sup>	ペタ	P	10 <sup>-6</sup>	マイクロ	μ
10 <sup>12</sup>	テラ	T	10 <sup>-9</sup>	ナノ	n
10 <sup>9</sup>	ギガ	G	10 <sup>-12</sup>	ピコ	p
10 <sup>6</sup>	メガ	M	10 <sup>-15</sup>	フェムト	f
10 <sup>3</sup>	キロ	k	10 <sup>-18</sup>	アト	a
10 <sup>2</sup>	ヘクト	h	10 <sup>-21</sup>	ゼプト	z
10 <sup>1</sup>	デカ	da	10 <sup>-24</sup>	ヨクト	y

表 3. 固有の名称とその独自の記号で表されるSI組立単位

組立量	SI 組立単位			
	名称	記号	他のSI単位による表し方	SI基本単位による表し方
平面角	ラジアン <sup>(a)</sup>	rad		m・m <sup>-1</sup> =1 <sup>(b)</sup>
立体角	ステラジアン <sup>(a)</sup>	sr <sup>(c)</sup>		m <sup>2</sup> ・m <sup>-2</sup> =1 <sup>(b)</sup>
周波数	ヘルツ	Hz		s <sup>-1</sup>
力	ニュートン	N		m・kg・s <sup>-2</sup>
圧力，応力	パスカル	Pa	N/m <sup>2</sup>	m <sup>-1</sup> ・kg・s <sup>-2</sup>
エネルギー，仕事，熱量	ジュール	J	N・m	m <sup>2</sup> ・kg・s <sup>-2</sup>
工率，放射束	ワット	W	J/s	m <sup>2</sup> ・kg・s <sup>-3</sup>
電荷，電気量	クーロン	C		s・A
電位差（電圧），起電力	ボルト	V	W/A	m <sup>2</sup> ・kg・s <sup>-3</sup> ・A <sup>-1</sup>
静電容量	ファラド	F	C/V	m <sup>-2</sup> ・kg <sup>-1</sup> ・s <sup>4</sup> ・A <sup>2</sup>
電気抵抗	オーム	Ω	V/A	m <sup>2</sup> ・kg・s <sup>-3</sup> ・A <sup>-2</sup>
コンダクタンス	ジーメン	S	A/V	m <sup>-2</sup> ・kg <sup>-1</sup> ・s <sup>3</sup> ・A <sup>2</sup>
磁束	ウェーバ	Wb	V・s	m <sup>2</sup> ・kg・s <sup>-2</sup> ・A <sup>-1</sup>
磁束密度	テスラ	T	Wb/m <sup>2</sup>	kg・s <sup>-2</sup> ・A <sup>-1</sup>
インダクタンス	ヘンリー	H	Wb/A	m <sup>2</sup> ・kg・s <sup>-2</sup> ・A <sup>-2</sup>
セルシウス温度	セルシウス度 <sup>(d)</sup>	℃		K
光束度	ルーメン	lm	cd・sr <sup>(c)</sup>	m <sup>2</sup> ・m <sup>-2</sup> ・cd=cd
照射度	ルクス	lx	lm/m <sup>2</sup>	m <sup>2</sup> ・m <sup>-4</sup> ・cd=m <sup>-2</sup> ・cd
（放射性核種の）放射能	ベクレル	Bq		s <sup>-1</sup>
吸収線量，質量エネルギー分与，カーマ線量当量，周辺線量当量，方向性線量当量，個人線量当量，組織線量当量	グレイ	Gy	J/kg	m <sup>2</sup> ・s <sup>-2</sup>
	シーベルト	Sv	J/kg	m <sup>2</sup> ・s <sup>-2</sup>

- (a) ラジアン及びステラジアンの使用は、同じ次元であっても異なった性質をもった量を区別するときの組立単位の表し方として利点がある。組立単位を形作るときにいくつかの用例は表 4 に示されている。
- (b) 実際には、使用する時には記号rad及びsrが用いられるが、習慣として組立単位としての記号“1”は明示されない。
- (c) 測光学では、ステラジアンの名称と記号srを単位の表し方の中にそのまま維持している。
- (d) この単位は、例としてミリセルシウス度m℃のようにSI接頭語を伴って用いても良い。

表 4. 単位の中に固有の名称とその独自の記号を含むSI組立単位の例

組立量	SI 組立単位		
	名称	記号	SI 基本単位による表し方
粘力のモーメント	パスカル秒	Pa・s	m <sup>-1</sup> ・kg・s <sup>-1</sup>
表面張力	ニュートンメートル	N・m	m <sup>2</sup> ・kg・s <sup>-2</sup>
角速度	ニュートン毎メートル	N/m	kg・s <sup>-2</sup>
角加速度	ラジアン毎秒	rad/s	m・m <sup>-1</sup> ・s <sup>-1</sup> =s <sup>-1</sup>
熱流密度，放射照度	ラジアン毎平方メートル	rad/s <sup>2</sup>	m・m <sup>-1</sup> ・s <sup>-2</sup> =s <sup>-2</sup>
熱容量，エントロピー	ワット毎平方メートル	W/m <sup>2</sup>	kg・s <sup>-3</sup>
質量熱容量（比熱容量），質量エントロピー（比エネルギー）	ジュール毎ケルビン	J/K	m <sup>2</sup> ・kg・s <sup>-2</sup> ・K <sup>-1</sup>
熱伝導率	ジュール毎キログラム毎ケルビン	J/(kg・K)	m <sup>2</sup> ・s <sup>-2</sup> ・K <sup>-1</sup>
体積エネルギー	ジュール毎立方メートル	J/m <sup>3</sup>	m <sup>-1</sup> ・kg・s <sup>-2</sup>
電界の強さ	ボルト毎メートル	V/m	m・kg・s <sup>-3</sup> ・A <sup>-1</sup>
体積電荷	クーロン毎立方メートル	C/m <sup>3</sup>	m <sup>-3</sup> ・s・A
電気変位	クーロン毎平方メートル	C/m <sup>2</sup>	m <sup>-2</sup> ・s・A
誘電率	ファラド毎メートル	F/m	m <sup>-3</sup> ・kg <sup>-1</sup> ・s <sup>4</sup> ・A <sup>2</sup>
透磁率	ヘンリー毎メートル	H/m	m・kg・s <sup>-2</sup> ・A <sup>-2</sup>
モルエネルギー	ジュール毎モル	J/mol	m <sup>2</sup> ・kg・s <sup>-2</sup> ・mol <sup>-1</sup>
モルエントロピー，モル熱容量	ジュール毎モル毎ケルビン	J/(mol・K)	m <sup>2</sup> ・kg・s <sup>-2</sup> ・K <sup>-1</sup> ・mol <sup>-1</sup>
照射線量（X線及びγ線）	クーロン毎キログラム	C/kg	kg <sup>-1</sup> ・s・A
吸収線量	グレイ毎秒	Gy/s	m <sup>2</sup> ・s <sup>-3</sup>
放射強度	ワット毎ステラジアン	W/sr	m <sup>4</sup> ・m <sup>-2</sup> ・kg・s <sup>-3</sup> =m <sup>2</sup> ・kg・s <sup>-3</sup>
放射輝度	ワット毎平方メートル毎ステラジアン	W/(m <sup>2</sup> ・sr)	m <sup>2</sup> ・m <sup>-2</sup> ・kg・s <sup>-3</sup> =kg・s <sup>-3</sup>

表 6. 国際単位系と併用されるが国際単位系に属さない単位

名称	記号	SI 単位による値
分	min	1 min=60s
時	h	1h =60 min=3600 s
日	d	1 d=24 h=86400 s
度	°	1° =(π/180) rad
分	′	1′ =(1/60)° =(π/10800) rad
秒	″	1″ =(1/60)′ =(π/648000) rad
リットル	l, L	1l=1 dm <sup>3</sup> =10 <sup>-3</sup> m <sup>3</sup>
トン	t	1t=10 <sup>3</sup> kg
ネーパ	Np	1Np=1
ベル	B	1B=(1/2) ln10 (Np)

表 7. 国際単位系と併用されこれに属さない単位でSI単位で表される数値が実験的に得られるもの

名称	記号	SI 単位であらわされる数値
電子ボルト	eV	1eV=1. 60217733 (49) ×10 <sup>-19</sup> J
統一原子質量単位	u	1u=1. 6605402 (10) ×10 <sup>-27</sup> kg
天文単位	ua	1ua=1. 49597870691 (30) ×10 <sup>11</sup> m

表 8. 国際単位系に属さないが国際単位系と併用されるその他の単位

名称	記号	SI 単位であらわされる数値
海里		1 海里=1852m
ノット		1 ノット=1 海里毎時=(1852/3600)m/s
アール	a	1 a=1 dam <sup>2</sup> =10 <sup>2</sup> m <sup>2</sup>
ヘクタール	ha	1 ha=1 hm <sup>2</sup> =10 <sup>4</sup> m <sup>2</sup>
バール	bar	1 bar=0. 1MPa=100kPa=1000hPa=10 <sup>5</sup> Pa
オングストローム	Å	1 Å=0. 1nm=10 <sup>-10</sup> m
バール	b	1 b=100fm <sup>2</sup> =10 <sup>-28</sup> m <sup>2</sup>

表 9. 固有の名称を含むCGS組立単位

名称	記号	SI 単位であらわされる数値
エルグ	erg	1 erg=10 <sup>-7</sup> J
ダイン	dyn	1 dyn=10 <sup>-5</sup> N
ポアズ	P	1 P=1 dyn・s/cm <sup>2</sup> =0. 1Pa・s
ストークス	St	1 St =1cm <sup>2</sup> /s=10 <sup>-4</sup> m <sup>2</sup> /s
ガウス	G	1 G ≐10 <sup>-4</sup> T
エルステッド	Oe	1 Oe ≐ (1000/4π) A/m
マクスウェル	Mx	1 Mx ≐10 <sup>-8</sup> Wb
スチルブ	sb	1 sb =1cd/cm <sup>2</sup> =10 <sup>4</sup> cd/m <sup>2</sup>
ホト	ph	1 ph=10 <sup>4</sup> lx
ガリ	Gal	1 Gal =1cm/s <sup>2</sup> =10 <sup>-2</sup> m/s <sup>2</sup>

表10. 国際単位に属さないその他の単位の例

名称	記号	SI 単位であらわされる数値
キュリー	Ci	1 Ci=3. 7×10 <sup>10</sup> Bq
レントゲン	R	1 R = 2. 58×10 <sup>-4</sup> C/kg
ラド	rad	1 rad=1cGy=10 <sup>-2</sup> Gy
レム	rem	1 rem=1 cSv=10 <sup>-2</sup> Sv
X線単位		1X unit=1. 002×10 <sup>-4</sup> nm
ガンマ	γ	1γ=1 nT=10 <sup>-9</sup> T
ジャンスキー	Jy	1 Jy=10 <sup>-26</sup> W・m <sup>-2</sup> ・Hz <sup>-1</sup>
フェルミ		1 fermi=1 fm=10 <sup>-15</sup> m
メートル系カラット		1 metric carat = 200 mg = 2×10 <sup>-4</sup> kg
トル	Torr	1 Torr = (101 325/760) Pa
標準気圧	atm	1 atm = 101 325 Pa
カロリ	cal	
マイクロン	μ	1 μ =1μm=10 <sup>-6</sup> m

